

Techno-Economic Analysis of a Hybrid Renewable Energy System in the Remote Areas in Kenya

Mulumba, Ngila Alphonce
九州大学大学院総合理工学府環境エネルギー工学専攻

<https://hdl.handle.net/2324/6788182>

出版情報：九州大学，2022，修士，修士
バージョン：
権利関係：



TECHNO-ECONOMIC ANALYSIS OF A HYBRID RENEWABLE ENERGY SYSTEM IN THE REMOTE AREAS IN KENYA

Alphonse Ngila Mulumba

Supervisor

Associate Professor. Hooman Farzaneh



FEBRUARY 1, 2023

Energy and Environmental Systems Laboratory,
Interdisciplinary Graduate School of Engineering Sciences

KYUSHU UNIVERSITY
Japan

Contents

List of Tables	3
List of Figures	3
Acknowledgment	6
1. Introduction	7
1.1 Overview of Energy situation in Kenya:	7
1.2 Community-based microgrid systems approach in Kenya:.....	9
1.3. Literature Review:.....	11
1.5 Research gap and originality highlights	15
2. Multi-objective optimization framework	17
2.1 HRES system composition:.....	17
2.2. Multi-objective optimization model:.....	17
2.3. Solving technique:.....	20
3. Mathematical modeling of the HRES components.....	23
3.1 Solar PV power generation:	23
3.1.1 Determination of panel orientation and radiation incident on the PV array:.....	23
3.1.2 Determination of PV cell temperature	24
3.1.3 Determination of PV power output	25
3.2 Wind turbine power generation model	25
3.3 Battery storage system modeling	26
3.4 Flywheel energy storage system modeling:	26
4. HRES dynamic power control simulation model	28
4.1. Internal model of PV cell:	28
4.2. Modeling the permanent magnet synchronous generator (PMSG) wind turbine:	29
4.3. Flywheel unit model in Matlab/Simulink:	31
4.4. Battery charge and discharge model:	33
4.5. Battery-Flywheel charge control method:.....	34
4.6. Perturb & Observe Algorithm for MPPT Technique:.....	35
4.7. Input data used in the simulation:	37
5. Results and Discussion	40
5.1 Area of study:.....	40
5.2 Optimal design of the proposed HRES:	41
5.3 Supply-demand balance during optimization.....	42

5.3.1 Scenario I.....	42
5.3.2 Scenario II.....	43
5.3.3 Scenario III.....	44
5.3.4 Scenario IV.....	45
5.3.5 Scenario V.....	45
5.4 HRES dynamic operation and simulation:.....	46
5.4.1. FESS frequency response advantage:.....	48
5.4.2 Battery capacity gain:.....	49
6. Conclusion.....	51
Appendix.....	53
Nomenclature.....	57
References.....	60

List of Tables

Table 1.1: Overview of related research papers on optimal sizing and dynamic power control	13
Table 4.1: solar panel parameters	38
Table 4.2: wind turbine parameters	39
Table 4.3: Battery parameters	39
Table 4.4: Flywheel parameters	39
Table 5.1: Optimization results	42
Table 5.2: Selected optimization scenarios	42
Table A-1: Recommended average days for months and values of n by months [42]	53

List of Figures

Figure 1.1: Kenya's electrical power generation portfolio	7
Figure 1.2: Access to electricity in Kenya	8
Figure 1.3: Electrical consumption summary in Kenya	8
Figure 1.4: Kenya's energy infrastructure; power stations, grid networks, potential energy sources, mini-grids, and population density by households	9
Figure 1.5: Mbogo valley micro-grid in rural Kenya	10
Figure 1.6: Access to electricity by % of the population in Sub-Saharan Africa	11
Figure 1.7: A comparison of Sub-Saharan African Countries' Access to Electricity by % of the population	11
Figure 1.8: Modeling framework in this study	15
Figure 2.1: schematic diagram of the composition of the HRES system.	17
Figure 2.2: Two-unit system illustration	19
Figure 2.3: Markov's time series reliability index curve	20
Figure 2.4: Optimization flow chart	22
Figure 3.1: Solar irradiance path on PV panel	23
Figure 3.2: Basic flywheel energy storage system layout	26
Figure 4.1: Schematic diagram of HRES System in Matlab/Simulink	28
Figure 4.2: The single diode model equivalent circuit for PV	29
Figure 4.3: wind turbine model energy conversion stages	30
Figure 4.4: Turbine power coefficient relationship to tip speed ratio	30
Figure 4.5: Matlab/Simulink flywheel model	32
Figure 4.6: SVPWM subsystem in flywheel model	33
Figure 4.7: Flywheel energy storage subsystem	34
Figure 4.8: Battery charging model	34
Figure 4.9: Flywheel-battery charge control scheme	35
Figure 4.10: P & O MPPT algorithm flowchart	35
Figure 4.11: DC-DC buck converter control circuit	36
Figure 4.12: Buck converter operation waveforms	37
Figure 4.13: I-V and P-V curves	38
Figure 4.14: Turbine Characteristics at $\beta = 0$	38

Figure 5.1: Schematic focus on the local area of research (Makueni, Nguu)	40
Figure 5.2: Hourly Electrical load profile for 72 hours in Makueni, Nguu.	40
Figure 5.3: Pareto frontier for the multi-objective ϵ -constraint solution	41
Figure 5.4: Pareto frontier for the multi-objective ϵ -constraint solution	42
Figure 5.5: Energy supply-demand balance for Scenario I.....	43
Figure 5.6: Energy supply-demand balance for Scenario II	44
Figure 5.7: Energy supply-demand balance for Scenario III.....	44
Figure 5.8: Energy supply-demand balance for the Scenario IV	45
Figure 5.9: Energy supply-demand balance for the Scenario V	46
Figure 5.10: Irradiance (w/m^2) and cell temperature (0C)	47
Figure 5.11: Wind Speed in m/s	47
Figure 5.12: Overall system performance for 72 hours of operation of the proposed HRES.	48
Figure 5.13: Flywheel-Battery system response to load demand at low solar/wind power generation.....	49
Figure 5.14: A comparison of the system's DOD with and without the FESS	50
Figure 5.15: State of charge (SOC) for the battery with and without the flywheel.....	50
Figure 5.16: Battery capacity gain with battery/flywheel storage system	50
Figure A-1: Annual hourly wind speeds in the Makueni area for 2021	53
Figure A-2: Annual hourly irradiance in Makueni for 2021.....	54
Figure A-3: Annual hourly ambient temperatures in Makueni area for 2021	54
Figure A-4: Tilt angle vs. power output variations for a 330Wp PV panel in 12 hours.....	54
Figure A-5: Radiation for the different scenarios	55
Figure A-6: Wind speed for different scenarios	55
Figure A-7: Annual energy supply-demand balance for 2021.....	56

Abstract

Sub-Saharan Africa (SSA) has the lowest energy access rates globally. The need for transformative energy sources ranging from solar off-grid and mini-grid solutions to hybrid micro-grid power systems has rapidly grown to deliver clean energy admittance. The accessibility of clean, reliable, affordable, and sustainable energy is important in any developing country and a great step towards sustainable development. This accelerates the need for community-based off-grid micro-grid power sources connected to energy storage systems to ensure affordable and optimally reliable electrical power. Such interventions are inevitable immediate solutions for remote and less accessible zones in SSA, acting as a golden thread to deliver on the promise of agenda 2030 sustainable development goals, SDGs.

This research proposes a hybrid Photovoltaic-Wind turbine Power System coupled to a hybridized storage system composed of a Lithium-Ion Battery and a Flywheel Storage System. The system ensures reliability for off-grid electrification for rural and less accessible remote areas of Makueni County in Kenya. A major ingenuity in this work is in carrying out a critical assessment and modeling an optimally sized PV/Wind/Battery/Flywheel power system whose fortitude is mapped on a multi-objective optimization modeling approach, taking into account the Levelized Cost of Electricity (LCOE) and reliability (energy index of self-reliance (EISR)) of the system as the main objective functions, using epsilon(ϵ)-constraint Technique as the solving approach. The optimal size estimated for the multi-objective optimization model is then used in a dynamic power control simulation model, which is developed in Matlab-Simulink to assess the hourly performance of the proposed HRES, under different operating conditions.

A resultant Pareto front is analyzed to obtain the best compromise for COE at 0.519 USD/kWh and reliability indicator, energy index of self-reliance (EISR) at 0.997. The optimal size of the HRES was realized at 26 PV panels (330 W) and 3 wind turbines (1 kW) which satisfies the annual local load requirement of 37.94MWh. Furthermore, adopting a hybrid energy storage system (HESS) shows a significant advantage in frequency response and gain in battery storage capacity during system operation. To demonstrate these two benefits, two states are analyzed during operation (1) during intermittency and (2) operation with HESS and with battery storage alone. The results show that the battery gains 858kWh capacity annually when coupled to the flywheel storage system.

Keywords: HRES, LCOE, EISR, Multi-objective optimization, Reliability, Pareto front, Epsilon(ϵ)-constraint technique, HESS, Flywheel, micro-grid, Maximum power point tracking

Acknowledgment

My sincere gratitude goes to Associate Prof. Hooman Farzaneh for his inexorable support and guidance as my supervisor throughout the research period. His patience, motivation, enthusiasm, and adorable knowledge eased my master's study and research work. I greatly appreciate the mentorship and advice under him during my master's study.

I also express my hearty appreciation to my family; my wife, Edith and our two sons (Israel & Joshua), who remained supportive, inspirational and a source of encouragement in my research.

I remain thankful to the Energy and Environmental Systems - Farzaneh laboratory members for their support and assistance during the research period.

Mulumba Alphonse Ngila

February 2023

Kyushu University, Chikushi Campus, Fukuoka, Japan

Chapter 1

Introduction

1.1 Overview of Energy situation in Kenya:

According to the 2022 daily system operation and dispatch analysis report by Energy and petroleum Regulatory Authority (EPRA) in Kenya, the country has a demand of 2,051MW against an installed generation capacity of 1,818MW (EPRA, 2021). Renewable energy sources in this installation contribute 88% of hydro, geothermal, wind, and solar capacity. Figure 1.1 illustrates Kenya's electrical power generation portfolio (EPRA, 2021). This demonstrates that solar power supplies 1% of the energy despite Kenya experiencing more than five overhead sun hours throughout the year. High dependence on hydropower sources has led to low power reliability in dry seasons. Only 71.4% of Kenya's population has access to electricity, with 62.7% accessibility in rural and remote areas, as described in Figure 1.2 (IEA, IRENA, UNSD, World Bank, 2022). The electricity demand is distributed according to Figure 1.1, which shows 31% in residential zones (ITA, 2022). The country has 99% of its existing off-grid electrification in rural and less accessible areas provided by small-scale stand-alone PV systems. Most of these privately owned installations are poorly mounted, resulting in supply-demand imbalance, especially during peak electrical demand hours. The government-installed mini-grids are powered mainly by solar and diesel generators providing backup during intermittence and night hours; this promotes greenhouse gas emissions.

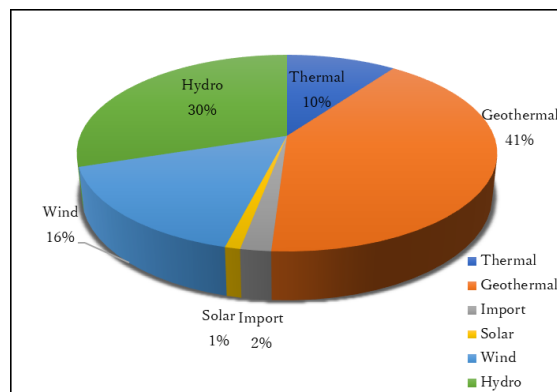


Figure 1.1: Kenya's electrical power generation portfolio

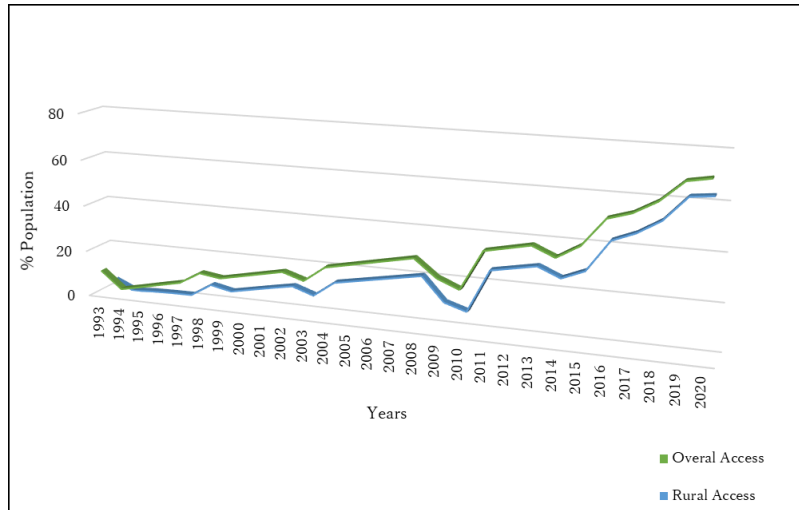


Figure 1.2: Access to electricity in Kenya

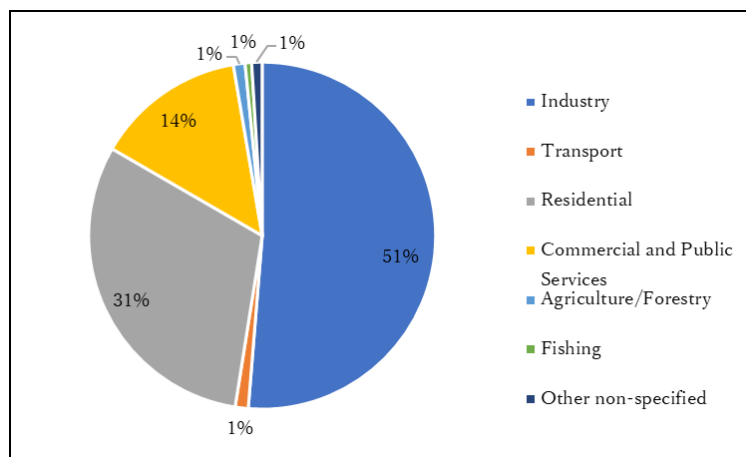


Figure 1.3: Electrical consumption summary in Kenya

The map in Figure 1.4 provides a detailed view of Kenya’s existing grid network, power plants, and decentralized mini-grids (EPRA, 2021). It shows the sparse distribution of power in remote areas with an advantageous concentration in urban areas. The poor levels of electricity accessibility in remote areas in Kenya give a strong reason for this research based on creating feasible, reliable, and practical demonstration for the effective implementation of an economical modern off-grid hybrid solar-wind system with the idyllic complementary storage system.

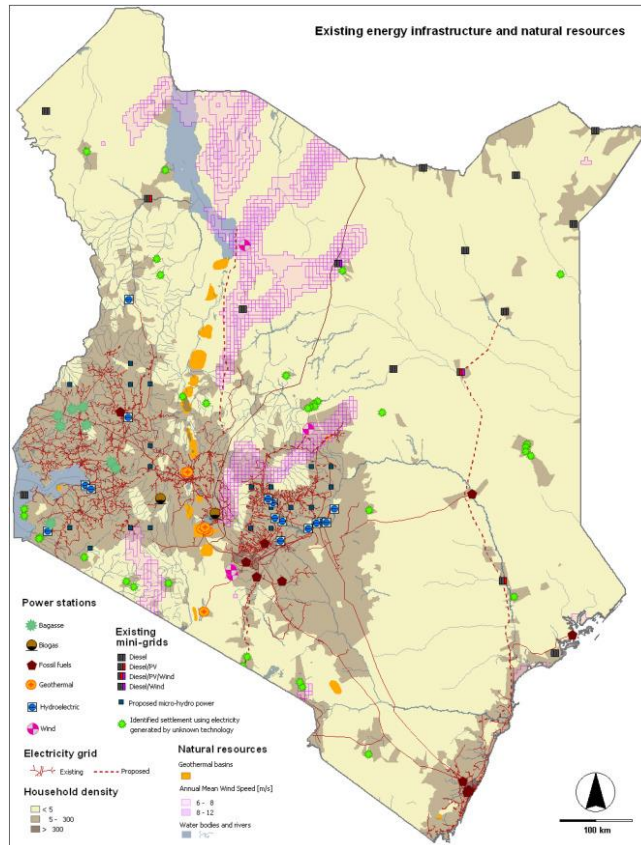


Figure 1.4: Kenya’s energy infrastructure; power stations, grid networks, potential energy sources, mini-grids, and population density by households

1.2 Community-based microgrid systems approach in Kenya:

The inaccessibility and isolation of rural communities in Kenya from grid networks and the lack of government-driven solutions to energy deficiency have led to community-driven microgrid initiatives (ITA, 2022). However, rural communities connected to the grid suffer frequent blackouts due to an unbalanced supply-demand curve in the country, low hydropower generation output in dry seasons, and intermittence in renewable energy sources. One example of such community-based microgrid systems in Kenya is featured in Figure 1.5 below (Projects, 2022). The solar/battery system is grid connected with 403kW rooftop photovoltaic installation and coupled to a 544kWh battery storage. A DC bus connects the solar system to a battery energy storage system (BESS) and a bi-directional grid forming a battery inverter. The Mbogo valley micro-grid is a viable example of a reliable community power system geared to alleviate energy poverty in a less accessible area in Kenya (Projects, 2022). This study absorbs the various benefits of this project and further proposes a more economical and reliable clean energy system in a similar locality in Kenya.

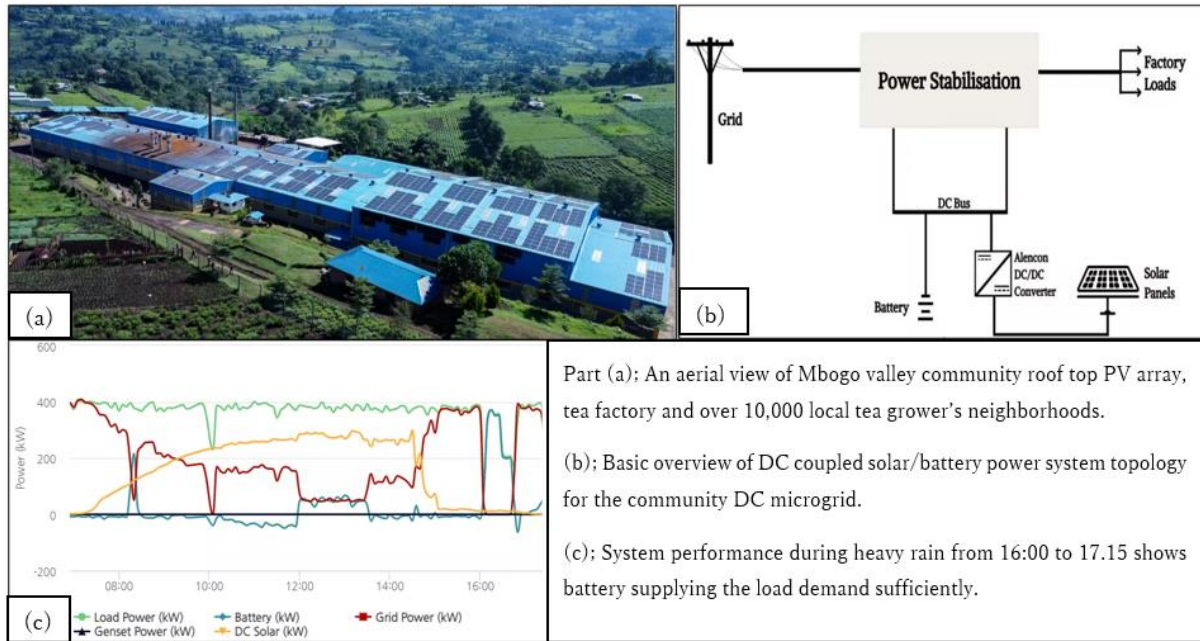


Figure 1.5: Mbogo valley micro-grid in rural Kenya

According to the world bank and the International Renewable Energy Agency (IRENA) tracking sustainable development goal 7 (SDG7) report for 2022 on energy progress, over 600 million people have no access to electricity, while 2.4 billion people are heavily dependent on unhealthy and environmentally harmful fuels for cooking and lighting (IEA, IRENA, UNSD, World Bank, 2022). Access to affordable, reliable, sustainable, and modern energy will be a dream far from reality for around 620 million people by 2030 (Projects, 2022). Figure 1.6 shows that more than 50% of the SSA population had no access to electricity in 2020. Figure 1.7 represents a comparison between different sub-Saharan African countries in the provision of access to electricity in 2020. Kenya has 71.4% of its population access to the national electrical grid network. Alarming, 80% of Kenyans in rural households use kerosene for lighting (EPRA, 2021). In the wake of these key insights, we can clearly assess the necessity for rapid growth in electricity generation in SSA driven by increased demand due to the rise in population and development in economic sectors. In addition, intensified fears of environmental impacts due to the high reliability of fossil fuels in urban and remote locations require imperative solutions (Ellabban, Abu-Rub, & Blaabjerg, 2014). Renewable energy generation and clean energy technologies are active character players in future renewable energy transitions (Shaqour, Farzaneh, Yoshida, & Hinokuma, 2020).

Integrating renewable energy sources and power storage is advantageous to creating affordable, reliable, and efficient power supply system (Höök & Tang, 2013). A hybrid system bearing a combination of solar and wind sources optimally attenuates substantial power fluctuations due to climate and meteorological conditions that result in high levels of the unreliability of RES power systems (Yazdanpanah, 2014). Conservative technological solutions provided by diesel generators are costly because of high fuel and maintenance costs.

On the other hand, agents of greenhouse gas emissions increase CO₂ levels in the atmosphere (Kaabeche & Ibtouen, 2014).

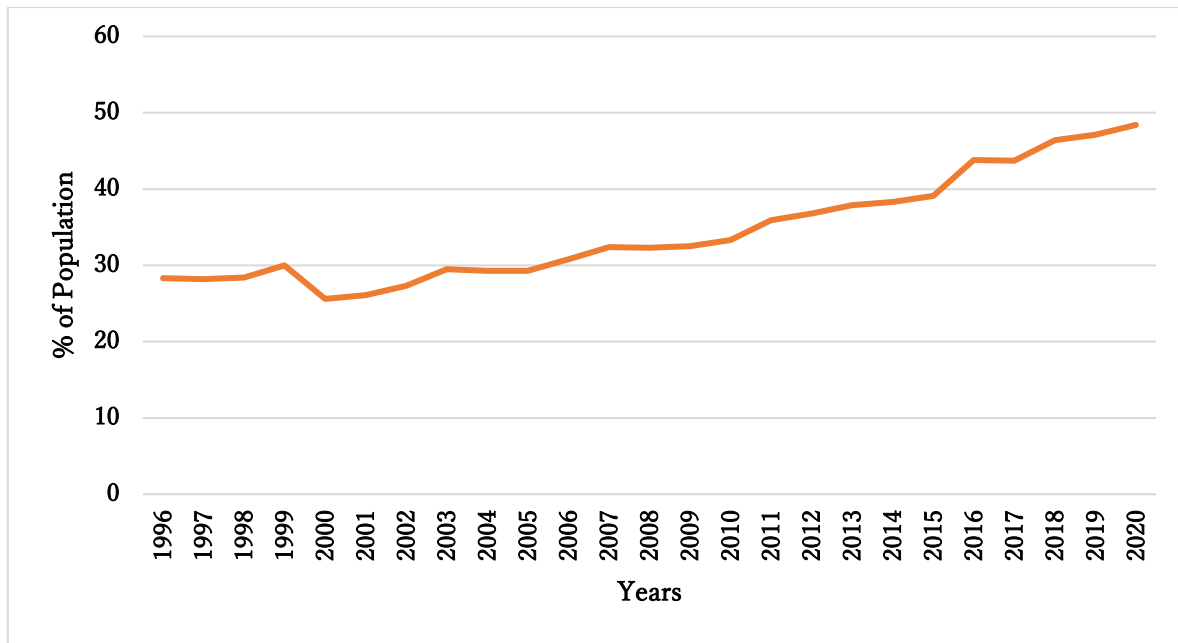


Figure 1.6: Access to electricity by % of the population in Sub-Saharan Africa

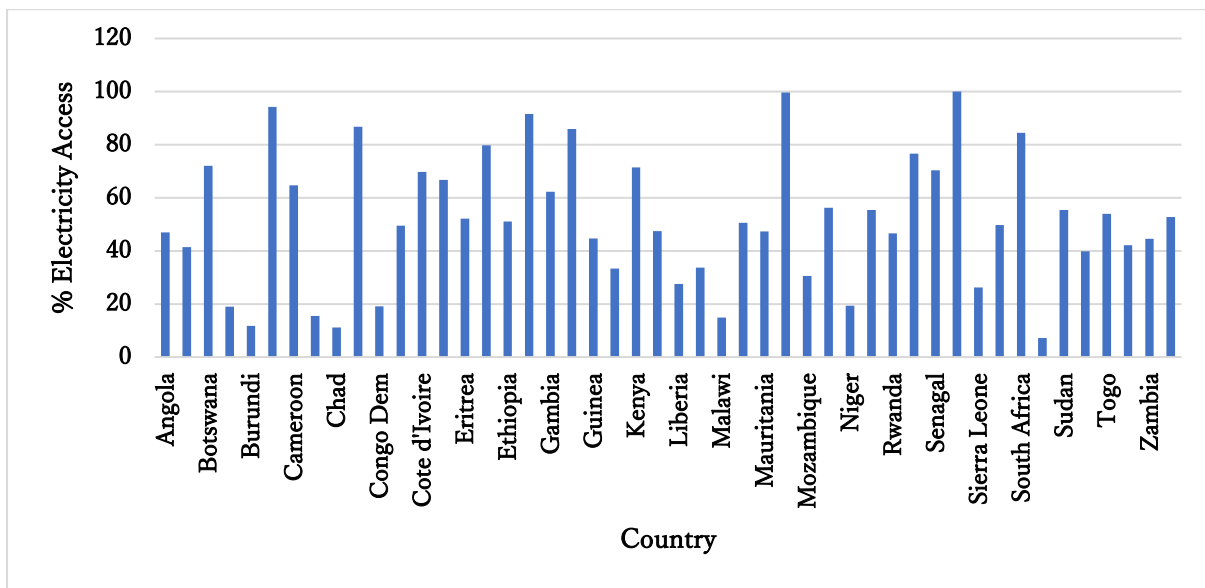


Figure 1.7: A comparison of Sub-Saharan African Countries' Access to Electricity by % of the population

1.3. Literature Review:

Off-grid microgrid hybrid renewable energy systems (HRES) combined with hybrid storage systems provide an accurate solution to power shortages in remote areas of the globe (Dehghani, Zhang, & Shafieezadeh, 2021). This can be ascribed to a lack of access to the utility grid, poor resource distribution, and an inability to balance supply and demand factors (Come Zebra, van der Windt, Nhumaio, & Faaij, 2021). Renewable energy microgrids are perfect

solutions to reducing greenhouse gases and augmenting the power supply and demand equation (Akbari, Vahidinasab, Arasteh, & Kazemi-Robati, 2022). Renewable systems like photovoltaics, wind turbines, battery, and flywheel storage have significantly low maintenance costs, emissions, reliability, and flexibility (Fathima & Palanisamy, 2015). The performance and reliability of HRES depend on the superlative synchronization and interaction between demand, generation output, efficiency aspects, storage, and the energy management strategy (Reinders et al., 2018). Further detailed scientific exploration into the performance features of the HRES system reveals unique specifications to polish prior to achieving an excellent output. Photovoltaic systems consist of structure modularity which helps attain ranges of generation scales from hundred watts to hundreds of megawatts. Optimal PV power yield, reliability, durability, integration, affordable costs, efficiency, and effectiveness are key factors in determining the maximum performance and optimization of solar modules of cost, size, and power demand (Bartolucci, Cordiner, Mulone, & Rossi, 2019).

Numerous studies have applied several algorithms to achieve multi-objective optimization and formulation of HRES systems. Such methods include particle swarm optimization (Amer, Namaane, & M'Sirdi, 2013), goal programming (Ramos, Boix, Montastruc, & Domenech, 2014), fuzzy logic approach (Khan, Pervez, Modibbo, Chauhan, & Ali, 2021), simulated annealing (W. Zhang, Maleki, Rosen, & Liu, 2018), and evolutionary genetic algorithms (Fadaee & Radzi, 2012), among other multi-objective optimization techniques. Fadaee et al. suggested various aspects or problem areas, including cost, reliability, design, and control, to be considered when optimizing stand-alone hybrid systems (Fadaee & Radzi, 2012). Previous research has been done to explain the sizing of the HRES system as a fundamental approach to addressing renewable energy fluctuation issues occasioned by intermittency. Abdullah Al-Shereiqli et al. articulated improvement on the scale of hybrid wind-solar power system hesitancy by sinking costs while simultaneously ensuring the obligation of power supply dependency. The paper explained two techniques for ensuring system reliability based on energy storage and a second control strategy (Al-Shereiqli, Al-Hinai, Albadi, & Al-Abri, 2021). Reena et al. considered the multi-objective optimization problem to minimize objectives on the operating cost of HRES, use of non-renewable energy resources, and fuel emission. The study compared single-objective and multi-objective optimization techniques in performing a trade-off (Sharma, Kodamana, & Ramteke, 2022). Ning et al. demonstrated a multi-objective optimal scheduling model using multi-objective particle swarm optimization (MOPSO) to describe the reversal relationship between LPSP and power supply reliability. Additionally, it propositioned the contribution of ESS towards improved reliability and enhanced penetration of distributed generation resources (N. Zhang, Yang, & Liu, 2021). This study borrowed heavily from these previous research works and further introduced the hybridization of storage as a perfect mechanism towards 100% system reliability. Table 1.1 outlines a comprehensive overview of related research papers and explains why their significant contribution is of great contribution to the novelty of this research work.

Table 1.1: Overview of related research papers on optimal sizing and dynamic power control

Ref	RES Type	Optimization Model	Significance/Contribution	Highlights
(Mahmoud et al., 2022)	Optimal sizing for PV/WTS/DGS/Battery System	Single Objective function optimization using different Algorithms; IGWO, GWO and SSA. Determines the annual cost and power supply deficiency in the optimization of system size	The optimum COE achieved is 0.21582 \$/kWh, with a preference for DGS sources due to low fuel cost. The efficiency of the optimization algorithms is 99.97%, 98.18% and 99.98% for IGWO, GWO and SSA. SSA has acceptable performance stability among the techniques.	This paper achieves low cost of electricity but gives preference to DGS, which is a source of CO ₂ . In this study, the flywheel and battery are optimally combined to eliminate the possible use of DGS during intermittence.
(Amer et al., 2013)	Hybrid Wind/PV/DG/Battery Power system	Particle swarm optimization technique (PSO), single objective optimization in LCE minimization.	The value of LCE obtained is 0.0030277 €/kW for a multisource HRES. The capacity of the turbine achieved is 1.0185kW and 0.23153kW for the PV module. Suggest preference to Wind power against PV and DG.	Considers smaller power demand not effectively reflecting changes in the cost of power and reliability, which may differ when a large residential power demand scenario is considered. The preference for wind over PV is not authenticated.
(Singh, Bansal, Singh, & Naidoo, 2018)	Hybrid Wind/PV/battery system	Multi-objective RESCA method was used to optimize the HRES system based on reliability and economic constraints	The size of the HRES system at minimum Annual system cost (ASC) represents 80.02% renewable energy fraction (REF). The composition in contribution for each energy source is shown by EGR = 1.08, which fairly shows the equal contribution of each source.	This research considers a pure, clean energy system and dwells on increasing reliability to 100%
(Alberizzi, Frigola, Rossi, & Renzi, 2020)	HRES system consisting of Solar, Wind, DG, and PTES/BESS storage	Optimal sizing using Mixed Integer Linear Programming (MILP) tool.	80.12% in cost savings is achieved using pumped thermal energy storage (PTES) to BESS. Reduction of HRES cost by 7.97%	Consideration of the flywheel storage system as a complementary storage to BESS brings about additional benefits in capacity gain and frequency.
(Ramli, Boucekara, &)	HMS; PV/Wind/DG/ Battery storage system	The multi-Objective Self-Adaptive	Achieves 95.51% in RF for optimum COE of 0.083\$/kWh and LSPS at	In this research, both optimization

Alghamdi, 2018)		Differential Evolution (MOSaDE) algorithm is used for optimal sizing, LPSP, and COE. A trade-off between two objectives was achieved with a Pareto front set of solutions for COE and LPSP.	0.219. The highest power contribution of power is from PV at 59%.	and operation are performed.
(Kamjoo, Maheri, Dizqah, & Putrus, 2016)	Stand-alone HRES comprising Wind Turbine, PV panel and Battery bank	Non-dominated Sorting Genetic Algorithm (NSGA-II) is utilized in solving multi-objective functions of system costs and reliability. The Chance Constrained Programming (CCP) method was proposed and validated to cater to RES uncertainties using Monte Carlo simulation.	Demonstrates that low costs DPSP (blackout probability) tends to be 100%. When DPSP is between 15% - 35%, we have the optimum COE. The optimal reliability index is 0.8.	This research seeks to demonstrate better reliability index results of 0.997.
(N. Zhang et al., 2021)	Hybrid Microgrid (PV/Wind/Battery)	Using Multi-objective particle swarm optimization (MOPSO) as a scheduling model for the minimization of Cost and maximize the reliability of power	Achieves maximum power reliability at the minimum value of LPSP. The COE and LPSP show a Pareto-trade-off with optimal COE between LPSP values of 2 – 8 %.	Contrary to the utilization of one storage method (BESS), this study proves higher reliability by adopting a hybrid storage system.
(Pang, Shi, Wang, & Pang, 2019)	Wind Power system with HESS (Battery and Supercapacitor)	Frequency-based optimal sizing (PPSO-GA) and control mechanism on MATLAB Simulink	Demonstrates a strong relationship between the cost of energy and battery cutoff frequency f_{bc} . The optimal cost is obtained at $f_{bc} = 1.623\text{MHz}$. Takes into consideration the impact of charge/discharge efficiency of the battery on the cost per day. Achieves a 59.62% decrease in COE and increases battery lifetime to 1.82 years.	This research focuses on using FESS to increase battery lifetime and improve system response frequency.

1.5 Research gap and originality highlights

Contrary to other research works explained earlier in which RES systems are optimized based on cost, this research dwells into multi-objective functions based on the comparison between cost and reliability, at the same time, authenticates the operation of the HRES system using actual climatic data to illustrate the dynamic power control process used. From Table 1.1, several papers have highlighted the methodology with little emphasis on the trade-off between reliability and COE, the use and significance of hybrid storage, and system operation control mechanisms.

To this aim, first, the research establishes a convergence of optimum cost and energy reliability for the HRES system, providing an appropriate size for PV panels, wind turbines, and energy storage based on the multi-objective ϵ -constraint mathematical programming. Secondly, it demonstrates a dynamic power operation using Matlab/Simulink simulation for the optimal sizes achieved in the optimization of the first part. A 72-hour simulation is carried out to illustrate the use of maximum power point tracking, MPPT-controlled HRES system with a unique hybrid energy storage system (HESS) made up of flywheel and battery, taking into account the accurate authentication using hourly data for irradiance, temperature, wind speed and actual residential power demand collected in Makueni which is the area of study to simulate the stand-alone system. This research proposes a perfect complementation by integrating PV and wind power generators. Optimal wind power is influenced by wind speed, air density, and blade radius wind (Akhavan Shams & Ahmadi, 2021). The combination of solar and wind power generators to obtain the optimum power output of the system considering the cost of components, installation, operation-maintenance, and storage costs, while minimizing possible situations of power un-reliability is a unique part of research figured out in this study. Figure 1.8 represents the overall structure of the modeling framework developed in this study, considering size optimization and operation management of the proposed HRES.

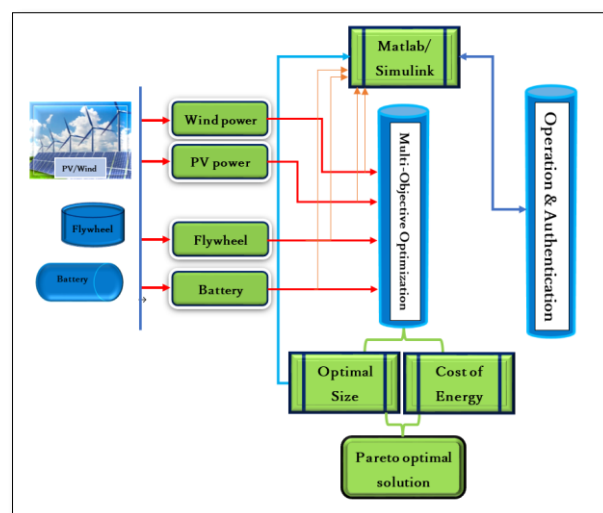


Figure 1.8: Modeling framework in this study

The thesis is structured as follows: Chapter 2 explains the multi-objective optimization framework for the HRES system. The model algorithm and solving technique are elucidated in detail. Chapter 3 expounds on the mathematical modeling envisaged in the system. This chapter

discourses in detail the scientific formation of the main components of the HRES system. Chapter 4 unveils the model of the dynamic power control simulation. The chapter demonstrates the system formation in Matlab. Chapter 5 details discussions of results during multi-objective optimization in GAMS and HRES operation in Matlab/Simulink. Chapter 6 describes the conclusion where the inferences and acclamations drawn from the research findings are abridged.

Chapter 2

Multi-objective optimization framework

2.1 HRES system composition:

The proposed HRES in this study includes photovoltaic modules, wind turbines on the supply side, and hybrid energy storage made up of a Li-ion battery and flywheel. Using hybrid storage systems in this study allows efficient storage complementation, increased duty cycles, and higher storage capacity.

The configuration of the proposed hybrid energy storage system (HRES) is shown in Figure 2.1. A common DC-link bus is used to reduce the cost and associated power losses significantly (Saleh, Awad, & Ghanem, 2019). Here the battery and flywheel energy storage systems are connected to the same bus (DC-link), eliminating the requirement for a DC-AC inverter for flywheel energy storage system (FESS), subsequently reducing the cost and associated power losses significantly (Saleh et al., 2019). The research illustrates the flywheel's effective spinning reserve for efficient backup power to the load eliminating the use of diesel generators (DGs), which are prone to carbon dioxide (CO₂) emissions. In addition, the flywheel adequately helps increase the lifetime of the battery by augmentation of more capacity and reduction of battery degradation. The use of FESS further serves to reduce possible adverse frequency swings in the system (Su, Jin, & Wang, 2010).

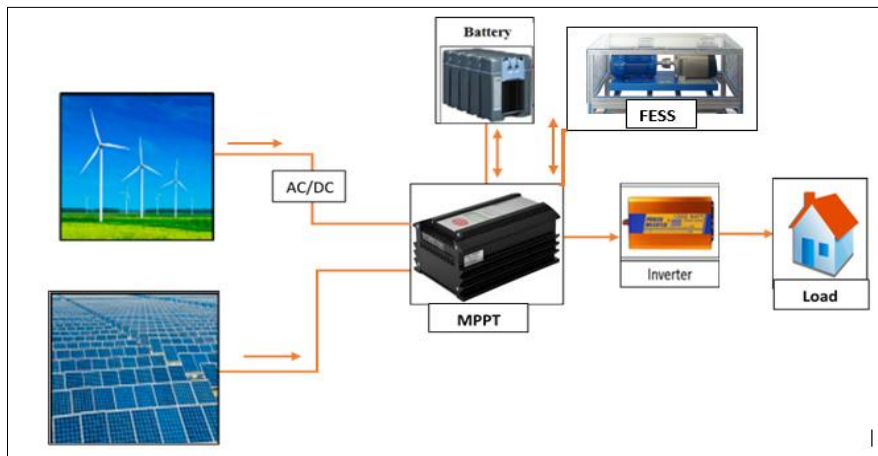


Figure 2.1: schematic diagram of the composition of the HRES system.

2.2. Multi-objective optimization model:

Solar and wind resources have inadequate power production proficiency due to their intermittency nature and high dependence on natural weather. On the other hand, the correct system size requires an accurate balance between power generation and demand. This means precision is vital in designing the solar/wind/battery/flywheel system to meet the electrical load demand while optimizing the cost and reliability of power. The study, therefore, develops a multi-objective optimization approach to determine the system's size, cost, and optimum reliability. The optimum solution enables desired decision in ensuring higher power reliability at affordable costs.

This research considers the economic and reliability aspect of the Hybrid renewable energy system by particularizing three major pieces of the power system. The formulation of optimal system size is based on cost of all components, installation, and operational costs. The optimum power reliability is based on the possible minimum cost of electricity. During optimization, two objectives with conflicting goals display the best compromise for the system's COE and reliability index.

The mathematical formulation for the multi-objective optimization model, which brings out a combined cost and reliability objective functions, is expressed as follows:

$$\text{Min } F(x) = \{f_1(\text{COE}), f_2(\text{UME})\} \quad (2-1)$$

This is subject to the following technical constraints:

Supply-demand balance constraint:

$$P_{PV(t)} + P_{WT(t)} + P_{\text{bat-discharge}(t)} + P_{\text{Fw-discharge}(t)} = P_{L(t)} + P_{\text{bat-charge}(t)} + P_{\text{Fw-charge}(t)} \quad (2-2)$$

Battery and Flywheel charging and discharging constraints:

$$P_{\text{bat-charge}(t)} + P_{\text{Fw-charge}(t)} = \begin{cases} \int_t^{t+\Delta t} ((P_{PV(t)} + P_{WT(t)}) - P_{L(t)}) dt & \text{if } (P_{PV(t)} + P_{WT(t)}) - P_{L(t)} > 0 \\ 0 & \text{if } (P_{PV(t)} + P_{WT(t)}) - P_{L(t)} \leq 0 \end{cases} \quad (2-3)$$

$$P_{\text{bat-discharge}(t)} + P_{\text{Fw-discharge}(t)} = \begin{cases} \int_t^{t+\Delta t} (P_{L(t)} - (P_{PV(t)} + P_{WT(t)})) dt & \text{if } (P_{PV(t)} + P_{WT(t)}) - P_{L(t)} < 0 \\ 0 & \text{if } (P_{PV(t)} + P_{WT(t)}) - P_{L(t)} \geq 0 \end{cases} \quad (2-4)$$

The total capital cost and annual operation and maintenance costs are summed, putting into consideration the Levelized Cost of Electricity generation (LCOE) from the proposed HRES as follows:

$$\text{COE} = \left(\frac{IC_i + RC_i + OMC_i}{(1+r)^y} \right) / \left(\frac{P_{Gen}}{(1+r)^y} \right) \quad (2-5)$$

The annual power generation, P_{Gen} from the HRES is expressed in the equation:

$$P_{Gen} = \sum_{t=1}^{8760} (P_{PV(t)} + P_{WT(t)} + P_{\text{bat-discharge}(t)} + P_{\text{Fw-discharge}(t)}) \quad (2-6)$$

The total annualized cost of the HRES can be calculated as follows:

$$IC = \sum_{t=1}^{8760} (P_{PV(t)} IC_{PV} + P_{WT(t)} IC_{WT} + P_{FW(t)} IC_{FW} + P_{\text{bat}(t)} IC_{\text{bat}}) \quad (2-7)$$

The unit costs, IC_{PV} , IC_{WT} , IC_{FW} , IC_{bat} for the PV, wind turbine, flywheel, and battery, respectively, are in [\$/kWh].

The unmet electricity index is considered in this research to measure the reliability aspect of the HRES system, which can be defined as follows:

$$UME_{(t)} = \sum_{t=1}^T \left\{ \frac{(P_{Bdch(t)} + P_{FWdch(t)} + P_{L(t)} - P_{WT(t)} - P_{PV(t)} - P_{Bch(t)} - P_{FWch(t)})}{P_{Gen(t)}} \right\} \quad (2-8)$$

The ability to minimize possible power inadequacies is virtuously anchored on the dynamic power-balancing capability of the system while ensuring reasonable economic implications (Camargo et al., 2019). To measure the reliability aspect of the HRES system, the Energy Index of Self-Reliance EISR is introduced based on the Markov model for reliability for a two-unit system (Kadri, Smaili, & Kadry, 2015)(shown in Figure 2.2).

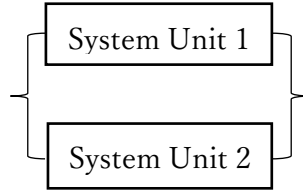


Figure 2.2: Two-unit system illustration

In this model, the system will perform its intended duty if either Unit 1, Unit 2, or both are operational. The model can be expressed by representing EISR using λ_{sys} such that the value of EISR determined using equation (2-9) has all equivalent variables articulated by equation (2-10).

$$\lambda_{sys} = \lambda_1 + \lambda_2 \quad (2-9)$$

$$\lambda_1 + \lambda_2 \leq 1 \quad (2-10)$$

In this case λ_1 is the failure rate of unit 1 and λ_2 is the failure rate of unit 2, as shown in Figure 2.2. For time-dependent or transient system analysis, determining the minimum acceptable system configuration for reliability within specified resource allocation, the value of λ_{sys} is obtained by accounting for possible failure to meet the system duty for a dynamic period.

$$\lambda_{sys} = LP_{(t)} \quad (2-11)$$

Where $P_{(t)}$ is a time-dependent preservation requirement for unit 1 and unit 2. L is a control value given by equation (2-12) while μ_1 and μ_2 represents operation efficiencies.

$$L = \mu_1 \lambda_1 + \mu_2 \lambda_2 \quad (2-12)$$

The value of λ_{sys} is exponentially illustrated as follows:

$$\lambda_{sys} = e^{M(t)} P_{(o)}(t) \quad (2-13)$$

$M(t)$ is a variable condition to be satisfied by the two states, while $P_{(o)}$ is an initial condition of $P_{(t)}$. Therefore, λ_{sys} , which represents the Energy Index of Self-Reliance EISR, assumes a predictable curve shown in Figure 2.3.

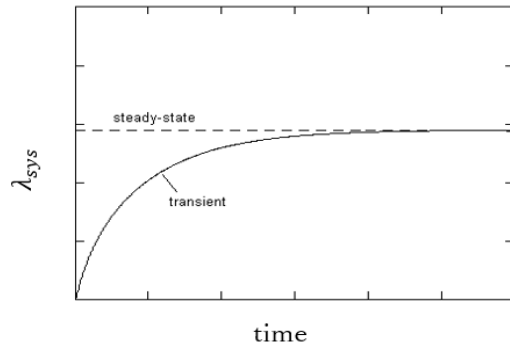


Figure 2.3: Markov's time series reliability index curve

Applying the Markov model in the HRES optimization scenario in this research helps in obtaining the measure of energy reliability. In this case, the UME is a time-dependent ratio representing the total unmet electricity demand for the hybrid system, considering two-unit states of power generation for PV and wind turbine and the amount of the discharged electricity to satisfy a residential electrical load demand. The Energy Index of Self-Reliance EISR is then introduced, using equation (2-14).

$$IESR_{(t)} = 1 - UME_{(t)} \quad (2-14)$$

When the value of EISR is always less than unity, when $EISR = 1$, this signifies the ideal or perfect reliability of the HRES system. The model intends to obtain an EISR value closer to unity. This means the multi-objective optimization model seeks to optimize both COE and UME functions to find the optimal configuration of the proposed HRES, where the cost of energy and unmet energy are minimized and the demand load requirement is fully satisfied.

2.3. Solving technique:

The ϵ -Constraint method is adopted as an efficient and modest optimization strategy for solving the multi-objective challenge. In this technique, one of the objective functions is selected, and the second objective function transforms to act as a restriction considering a specific constraint, epsilon (ϵ) (Bérubé, Gendreau, & Potvin, 2009). Introducing different values of ϵ , results for optimal Pareto solutions are obtained through the utilization of a mixed-integer algorithm in a non-linear environment generating Pareto feasible and non-dominated solutions (Michanan, Dewri, & Rutherford, 2015).

The functions $f_{1(COE)}$ and $f_{2(UME)}$ are treated as constraints in the epsilon-constraint method in sequence. Hence, the model optimizes one objective function while keeping the other objective function within certain set proximities of deviation. For an allowable selected

range of ε ; Therefore, the multi-objective optimization model can be re-written in the following format:

$$\text{Min } f_{1(\text{COE})} \tag{2-15}$$

Subject to:

$$\left\{ \begin{array}{l} f_{2(\text{UME})} \leq \varepsilon_1 \\ \vdots \\ \vdots \\ f_{k\text{min}} \leq \varepsilon \leq f_{k\text{max}} \end{array} \right. \quad \text{Technical constraints}$$

Where, $f_{k\text{min}}$ and $f_{k\text{max}}$ represent a range of all objective functions formulated as a result of adopting changing values of ε and therefore used as constraints. This creates a lexicographic series of objective function optimization where the initial objective function solution is obtained then among the possible alternative optima; the algorithm optimizes for the second or subsequent objective function (Mavrotas, 2009). Thus, in every optimum solution where $f_{1(\text{COE})} = x_1$ for a selected epsilon value ε_1 , there is a corresponding $f_{2(\text{UME})} = x_1''$ for values in the range of $f_{k\text{min}} \leq \varepsilon_1 \leq f_{k\text{max}}$.

The multi-objective optimization algorithm in GAMS is demonstrated in Figure 2.4. The renewable energy inputs used to generate the overall power output and optimization procedure based on the HRES system parameters, constraints, and electricity demand for the study area are described in the flowchart. HESS charging and discharge conditions are exposed as governing the ability of the system to sustain the demand while upholding the minimum cost of electricity reliably.

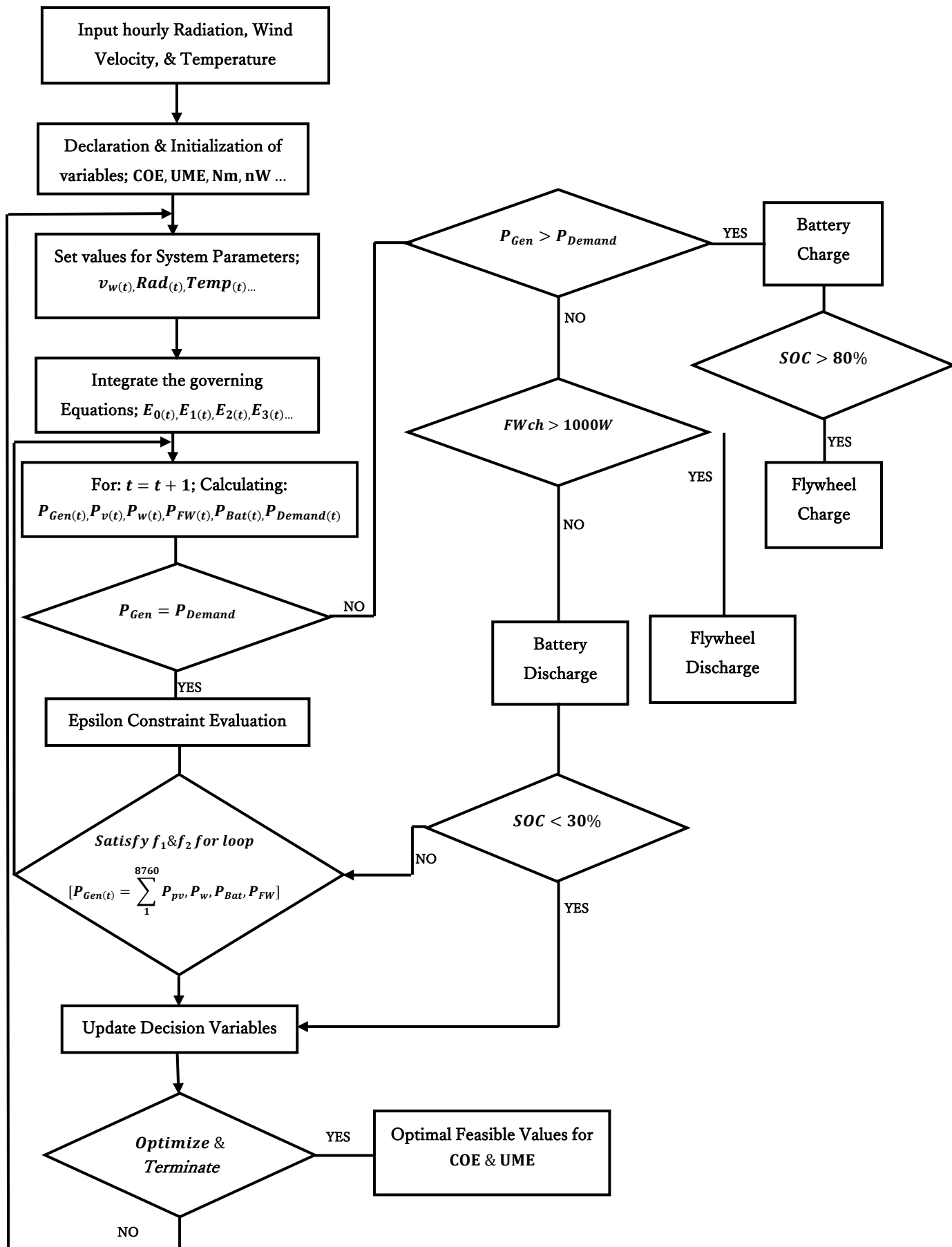


Figure 2.4: Optimization flow chart

Chapter 3

Mathematical modeling of the HRES components

3.1 Solar PV power generation:

Africa enjoys 51% of the earth's most concentrated sunlight. This means the rest of the world receives only 49% share. Kenya lies astride the equator, receiving normal direct radiation (DNI) levels averaging 4.5kWh/m²/day. Despite the substantial DNI levels, Kenya has only less than 2% power share extracted from solar. Makueni lies approximately 2° to the south of the equator. To reduce possible shading losses, this study details the accurate determination of a precise orientation angle (Duffie, Beckman, & McGowan, 1985). A stepwise focus for the elaboration of the photovoltaic model in this research entails:

- Determination of panel orientation and radiation incident on the PV array
- Determination of PV cell temperature
- Determination of PV power output

3.1.1 Determination of panel orientation and radiation incident on the PV array:

The relationship between the sun path and solar panel can be demonstrated in Figure 3.1. For a chosen solar panel orientation, the solar radiation angle of incidence depends on time, latitude, and panel alignment (Duffie et al., 1985). In this figure, \vec{E} , \vec{S} , \vec{Z} , \vec{n} , are representative vectors for South direction, East direction, zenith vector orthogonal to the plane of SE and normal to the panel plane, respectively.

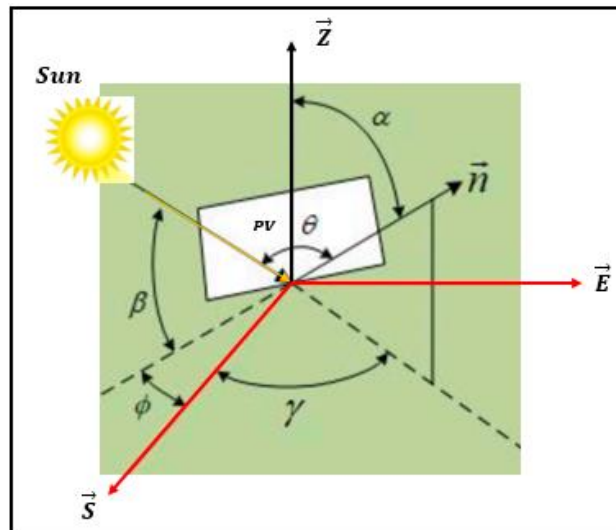


Figure 3.1: Solar irradiance path on PV panel

The relationship of the solar PV panel tilt angle α , solar azimuth angle φ , and surface azimuth angle γ , for a beam of radiation incident to a surface, can be expressed by the equation (3-1) below (Ben hmamou et al., 2022).

$$\cos\theta = \cos\beta\cos(\varphi - \gamma)\sin\alpha + \sin\beta\cos\alpha \quad (3-1)$$

As described in Figure 3.1, the angle between incident radiation and the normal to the panel is θ . The solar altitude angle β is obtained using equation (3-2), shown below

$$\sin\beta = \cos l \cos h \cos\delta + \sin l \sin\delta \quad (3-2)$$

The value of the local latitude is given by l , and the hour angle h is derived from

$$h = \frac{360}{24} \times (T - 12) \quad (3-3)$$

The solar time, T , is calculated by equation (3-4) where L_{st} and L_{loc} refer to standard longitude and local longitude, respectively (Ben hmamou et al., 2022).

$$T = \text{standard time} + [4(L_{st} - L_{loc}) + EOT]/60 \quad (3-4)$$

and

$$EOT = -9.87\sin 2n + 7.53\cos n + 1.5\sin n \quad (3-5)$$

The solar declination angle δ is found through approximation using equation (3-6).

$$\delta = 23.45\sin\left(360\frac{284+n}{365}\right) \quad (3-6)$$

The recommended average days for months and values of n by months used in this research have been tabulated in Table A-1 at the appendix.

The solar azimuth angle is biased to the direction of the incident beam, which is positive for the western-facing panel, negative for the eastern, and zero for south facing panel. The value can therefore be determined using equation (3-7).

$$\varphi = (-1)^s \cos^{-1}\left(\frac{\sin\beta\sin l - \sin\delta}{\cos\beta\cos l}\right) \quad (3-7)$$

The proponent $s = 1$ for solar morning hours, $s = 2$ for solar afternoons, and during solar noon the value of $\varphi = 0$.

The solar radiation data from Makueni is obtained and tabulated for diffuse horizontal incident (DHI) radiation from the direct normal incident (DNI) and global Horizontal Incident (GHI) using the equation shown in (3-8) (Ben hmamou et al., 2022).

$$DHI = GHI - DNI\sin\beta \quad (3-8)$$

The total insolation striking the panel is determined using the function expressed in equation (3-9).

$$I_T = DNI\cos\theta + DHI\left(\frac{1+\cos\alpha}{2}\right) + GHI\left(\frac{1-\cos\alpha}{2}\right) \quad (3-9)$$

3.1.2 Determination of PV cell temperature

The photovoltaic cell temperature varies for different times of the day; at night, it's equal to the ambient temperature, while huge variations are witnessed during sun hours (Duffie et al., 1985). The value for T_c is determined via the equation below.

$$T_c = T_a + \frac{G_g}{G_o} (T_{NOCT} - 20) \quad (3-10)$$

3.1.3 Determination of PV power output

To obtain the best tilt angle, the output of the PV array is calculated by the following equation (3-11) (Al-Shereiqi et al., 2021). In this case, the nominal PV power output value is obtained from the solar panel manufacturer's nameplate value.

$$P_{pv(t)} = G_{pv} f_{pv} \left(\frac{I_{T(t)}}{I_{T,STC}} \right) [1 + \alpha_p (T_{c(t)} - T_{c,STC})] \quad (3-11)$$

The values of P_{pv} from one panel rated at 330Wp is obtained based on each month of the chosen year (2021), for random days and hours. These results are visualized and used to determine the best orientation of the photovoltaic panel. Figure A-4 illustrates the outputs obtained for different hours around the day.

3.2 Wind turbine power generation model

The power generated by the wind turbine is on accounts for the conversion of the wind's kinetic energy to electrical energy (Huang, Shi, Wang, Lu, & Cui, 2015). This happens in three stages; the aerodynamic stage, in which moving air is converted into mechanical energy, and the mechanical stage comprising torque speed transforming into an electrical power constituent. The functional factors here are turbine size, wind speed, and the height of the rotor (Huang et al., 2015), (Hasan & Genç, 2022), the relationship is explained using the following equations:

$$v = v_{ref} \left(\frac{h_{hub}}{h_{ref}} \right)^\alpha \quad (3-12)$$

The wind speed v is directly proportional to the wind speed at the reference height, v_{ref} and the turbine height h_{hub} , while the reference height h_{ref} is inversely proportional. The power law coefficient α , fluctuates between 0.1 to a value equal to or slightly higher than 0.25 in cases of flat land to highly vegetative areas duly determined by terrain, height, season, wind speed variations, day, and hour within a specified geographical context. The power generated by the wind turbine at the time, t ($P_{WT(t)}$) is obtained as below (Mavrotas, 2009):

$$P_{WT(t)} = \begin{cases} 0 & v_{cut_out} < v(t) < v_{cut_in} \\ v(t)^3 \left(\frac{P_{rated}}{v_{rated}^3 - v_{cut_in}^3} \right) - P_{rated} \left(\frac{v_{cut_in}^3}{v_{rated}^3 - v_{cut_in}^3} \right) & v_{cut_in} \leq v(t) < v_{rated} \\ P_{rated} & v_{rated} \leq v(t) < v_{cut_out} \end{cases} \quad (3-13)$$

The rated power of the turbine is achieved at v_{rated} , this is a suitable compromise between v_{cut_in} at which generation starts and v_{cut_out} when the turbine shuts down to avoid damage (Hasan & Genç, 2022).

3.3 Battery storage system modeling

Renewable energy microgrids are more reliable when coupled with a sound and efficient energy storage system. This is due to variations and unpredictability in solar radiation and wind speeds. When the energy produced by the HRES, $E_{gen(t)}$ surpasses the electrical load, $E_L(t)$, the surplus energy is stored in battery bank storage according to equation (3-14) stated below (Pang et al., 2019).

$$E_{bat(t)} = E_{bat(t-1)} + (E_{gen(t)} - E_L(t)) \quad (3-14)$$

Where $E_{bat(t)}$ is the energy stored in the battery at time t, $E_{bat(t-1)}$ is energy stored in the battery at time $(t - 1)$, (N. Zhang et al., 2021). At any time, t the value of E_{bat} satisfies the constraint:

$$E_{bat_min} \leq E_{bat(t)} \leq E_{bat_max} \quad (3-15)$$

Using the charge transfer in and out of the battery, the *SOC* will be examined (N. Zhang et al., 2021). The battery discharge, P_{bat_disch} is used to accommodate variations during battery duty cycles (Colmenar-Santos, Monteagudo-Mencucci, Rosales-Asensio, de Simón-Martín, & Pérez-Molina, 2019).

$$SOC(t) = SOC(t_0) - \frac{1}{P_{bat_disch}} \int_0^t I_{bat(t)} dt \quad (3-16)$$

3.4 Flywheel energy storage system modeling:

Flywheel is a kinetic-dependent energy storage technology (Andy, Tameghe, & Wamkeue, 2015). Energy is stored in a rotating mass depending on the speed of the rotor mass, shape, and angular speed of revolution. The use of vacuum containment and bearings eliminates friction due to rotation. When charging, electric energy is supplied to the stator winding, converted to torque, and applied to the rotor, which spins to gain kinetic energy. During discharge, kinetic energy stored in the rotor applies a torque which in turn is converted to electric energy.

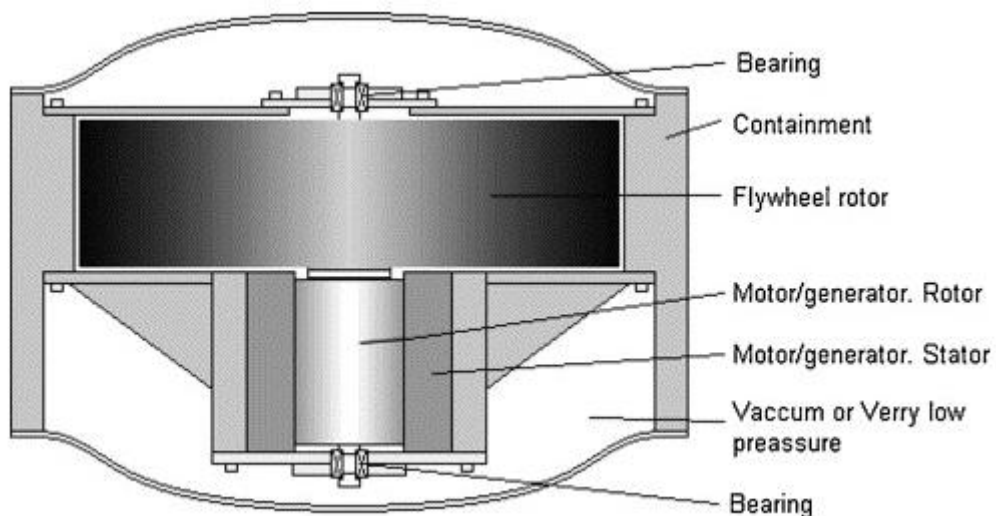


Figure 3.2: Basic flywheel energy storage system layout(Kovalev, Poltavets, & Kolchanova, 2019)

The kinetic energy stored is linearly proportional to the moment of inertia and the square of its angular velocity as in equation (3-17).

$$E_{FW} = \frac{1}{2}I\omega_f^2 \quad (3-17)$$

Here, E_{FW} is the stored kinetic energy, I is the moment of inertia, and ω_f is the angular velocity of the flywheel. The moment of inertia is a function of the mass of rotor and the rotor shape factor, therefore; outer radius r_o , inner radius r_i , height h and the mass density ρ relate according to equation (3-18).

$$E_{FW} = \frac{1}{2}\pi\rho h\omega_f^2(r_o^2 - r_i^2) \quad (3-18)$$

When materials with high strength-to-weight ratios are utilized, the bearing losses become negligible. Fused materials such as carbon fiber have the desired properties for high-speed, high-power density, compact design, high energy efficiency, low heat output, high uptime availability, and low-cost maintenance.

The flywheel safely operates within ω_{fmax}^2 and ω_{fmin}^2 to limit voltage variation and maximum torque for a given power rating (Olabi, Wilberforce, Abdelkareem, & Ramadan, 2021). Therefore, the useful energy of a flywheel is defined within maximum and minimum angular velocity, ω_f :

$$P_{FW(t)} = \frac{1}{2}I(\omega_{fmax}^2 - \omega_{fmin}^2) \quad (3-19)$$

Chapter 4

HRES dynamic power control simulation model

The schematic diagram in Figure 4.1 shows the HRES Matlab simulation architectural structure. The system utilizes a hybrid model of P&O MPPT to ensure optimal power output for both PV and Wind turbines. The output power satisfies the demand via a DC-DC buck converter and further speeds up the charging of the battery and flywheel.

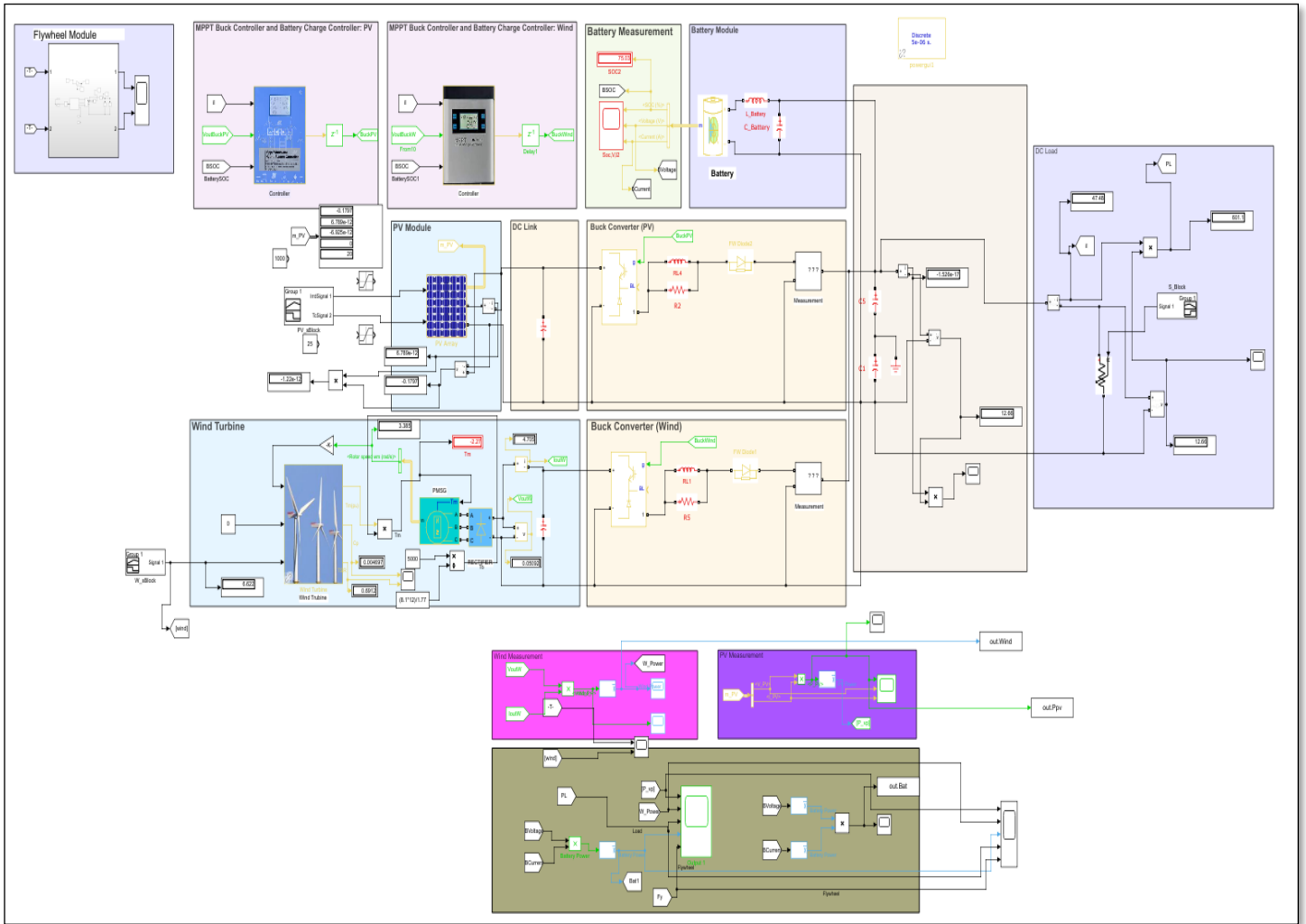


Figure 4.1: Schematic diagram of HRES System in Matlab/Simulink

4.1. Internal model of PV cell:

The intensity of solar radiation and ambient temperatures are important factors in PV power generation. A simple five-parameter ideal photovoltaic cell is represented in Figure 4.2. The photovoltaic current, because of incident radiation, is I_{ph} , the reverse current due to the PN junction of the solar cell is represented by I_D while R_p and R_s is the shunt and series resistances, respectively (Ishwarya, Yasoda, & Info, 2020).

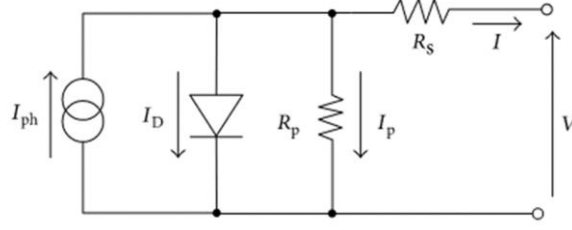


Figure 4.2: The single diode model equivalent circuit for PV(Jacob & Farzaneh, 2022).

The I-V characteristic of the PV model is determined by the application of Kirchoff's current law (KCL)

$$I = I_{ph} - I_D - I_{sh} \quad (4-1)$$

To consider all five PV cell parameters, the equation is formulated as follows.

$$I = I_{ph} - I_o \left[\exp \left(\frac{V+IR_s}{a} \right) - 1 \right] - \frac{V+IR_s}{R_p} \quad (4-2)$$

The modified ideality factor a refers to the physical constants expressed in the function below:

$$a = \frac{nkT^*N_s}{q} \quad (4-3)$$

The solar panel parameters defined by the manufacturer include $N_s, I_{mp}, V_{mp}, I_{sc}, V_{oc}$ which can be used to determine the five parameter requirement; I_{ph}, I_o, R_s, R_p, a . These are defined depending on the cell temperature and solar radiation. Using the iteration method into equation (4-4) and extracting the values of the short circuit current I_{sc} , open circuit voltage V_{oc} , and maximum power points from I-V characteristic curve, the five parameters are obtained (Jacob & Farzaneh, 2022).

The PV power output is given by the equation below:

$$P_{pv} = IV \quad (4-4)$$

4.2. Modeling the permanent magnet synchronous generator (PMSG) wind turbine:

A wind turbine converts the wind energy to mechanical energy, which further runs the generator to obtain electrical power, Figure 4.3 (Yang, Zhou, Lu, & Fang, 2008). The mechanical power generated by a wind turbine can be expressed as(4-5).

$$P_m = \frac{1}{2} C_p(\lambda, \beta) \rho A u^3 \quad (4-6)$$

The wind turbine λ is given by the following equation.

$$\lambda = \frac{r_m \omega r}{u} \quad (4-7)$$

The power coefficient, C_p , describes the power extraction efficiency of the wind turbine. It is a nonlinear function of both the tip speed ratio, λ and the blade pitch, β as revealed in Figure 4.4. While its maximum theoretical value is approximately 0.59, it is practically in this study,

the highest value is 0.48 at $\beta = 0^\circ$ and $\lambda = 8.1$. There are several versions of equations for C_p according to different literatures, a generic equation based on the modeling turbine characteristics is shown as follows (N. Zhang et al., 2021):

$$C_p(\lambda, \beta) = 0.5176 \left(116 * \frac{1}{\lambda_i} - 0.4\beta - 5 \right) e^{-\frac{21}{\lambda_i}} + 0.0068\lambda \quad (4-8)$$

With

$$\frac{1}{\lambda_i} = \frac{1}{\lambda + 0.08\beta} - \frac{0.035}{1 + \beta^3} \quad (4-9)$$

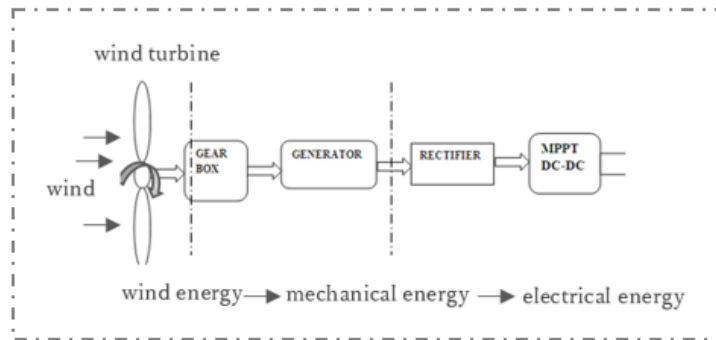


Figure 4.3: wind turbine model energy conversion stages(N. Zhang et al., 2021)

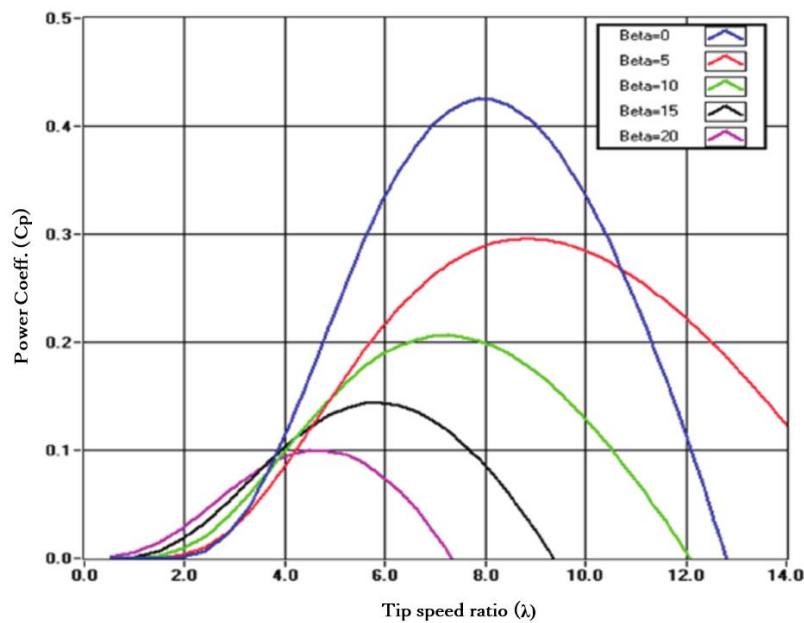


Figure 4.4: Turbine power coefficient relationship to tip speed ratio(Shaqour et al., 2020)

PMSG wind turbines are efficient for low-speed direct drive because they can have a higher pole number of 60 or more poles conventional wound rotor synchronous generators (Jacob & Farzaneh, 2022). The $d - q$ reference rotating frame for the dynamic model of the PMSG wind turbine is expressed using the equations:

$$\frac{d\psi_{sd}}{dt} = -V_{sd} - R_s I_{sd} - \omega_m \psi_{sq} \quad (4-10)$$

$$\frac{d\psi_{sq}}{dt} = -V_{sq} - R_s I_{sq} - \omega_m \psi_{sd} \quad (4-11)$$

Considering the above equations:

$$\psi_{sd} = (L_{sd} - L_{md})I_{sd} + \psi_m \quad (4-12)$$

$$\psi_{sq} = (L_{sq} + L_{mq})I_{sq} \quad (4-13)$$

Since the rotor is round, the phase inductances in equations (4-14) and (4-15) do not vary, and therefore equation (4-16) is true.

$$L_d = L_{sd} + L_{md} \quad (4-14)$$

$$L_q = L_{sq} + L_{mq} \quad (4-15)$$

$$L_d = L_q = \frac{L_{ab}}{2} \quad (4-16)$$

The PMSG active and reactive power is given by

$$P_s = V_{sd}I_{sd} + V_{sq}I_{sq} \quad (4-17)$$

$$Q_s = V_{sq}I_{sd} - V_{sd}I_{sq} \quad (4-18)$$

The wind PMSG generator torque with the number of pole pairs is given by equation (4-19).

$$T_e = 0.5\rho(\psi_m I_{sq} + (L_d - L_q)I_{sd}I_{sq}) \quad (4-19)$$

The torque and rotor angular velocity is expressed in the following equations.

$$\frac{d}{dt}\omega_m = \frac{1}{J}(T_e - T_f - F_{\omega_m} - T_m) \quad (4-20)$$

$$\frac{d\theta}{dt} = \omega_m \quad (4-21)$$

4.3. Flywheel unit model in Matlab/Simulink:

The flywheel uses the electromechanical principle to store energy (Su et al., 2010). A motor is used to convert electrical energy from the source into mechanical energy. The same motor is used as a generator during flywheel discharge to provide electrical energy. The flywheel model in Matlab/Simulink is shown in Figure 4.5. It is composed of a permanent magnet synchronous machine, space vector pulse width modulation, and energy storage subsystem.

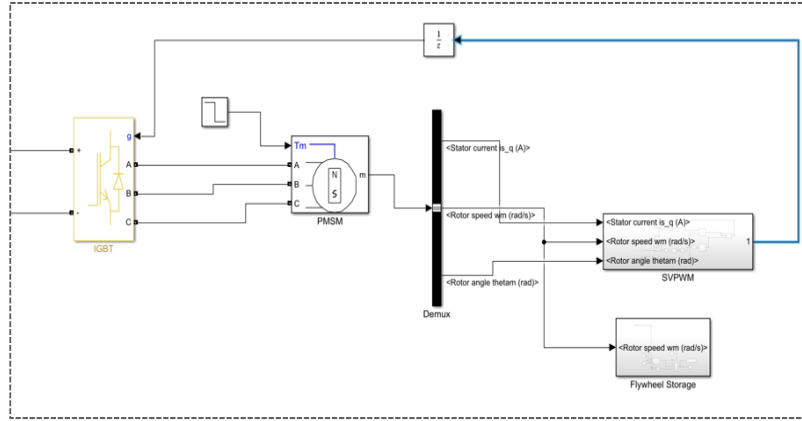


Figure 4.5: Matlab/Simulink flywheel model

The motor/generator is modeled as a permanent magnet synchronous machine (PMSM), as shown in Figure 4.5. The electrical system is expressed using the equations:

$$\frac{d\psi_{sd}}{dt} = -V_{sd} - R_s I_{sd} - \omega_m \psi_{sq} \quad (4-22)$$

$$\frac{d\psi_{sq}}{dt} = -V_{sq} - R_s I_{sq} - \omega_m \psi_{sd} \quad (4-23)$$

$$T_e = 0.5\rho(\psi_m I_{sq} + (L_d - L_q)I_{sd}I_{sq}) \quad (4-24)$$

The mechanical system is expressed by equations:

$$\frac{d}{dt} \omega_m = \frac{1}{J} (T_e - T_f - F_{\omega_m} - T_m) \quad (4-25)$$

$$\frac{d\theta}{dt} = \omega_m \quad (4-26)$$

Space vector pulse width modulation (SVPWM) applies a modulation scheme for a given voltage vector that emulates a three-phased sinusoidal waveform providing frequency and amplitude control. Using a Clarke-park transformation, we achieve a two-dimensional d-q frame. The “d” component represents the flux, and the “q” component represents the torque. PI controllers are used to obtaining speed regulation and proportional plus integral PI for current regulation. The SVPWM subsystem is shown in Figure 4.6. Energy storage in the flywheel is illustrated by equation (3-17) explained earlier. The flywheel energy storage subsystem is illustrated in Figure 4.7.

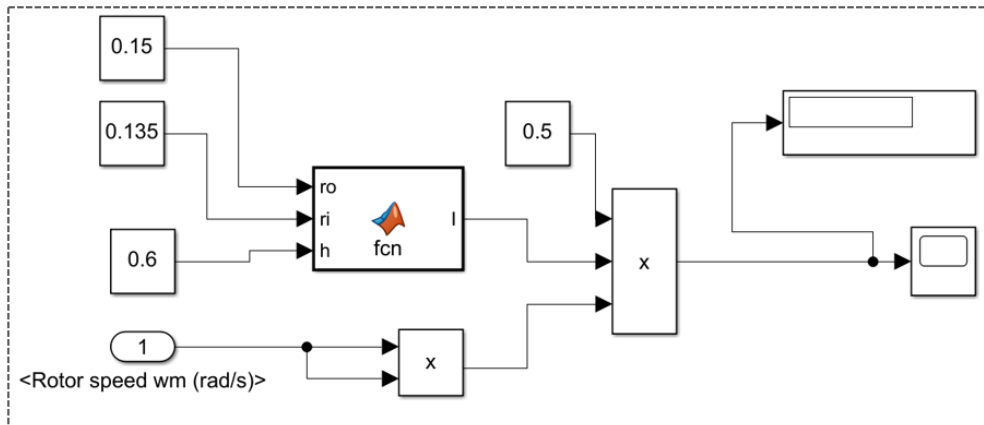


Figure 4.7: Flywheel energy storage subsystem

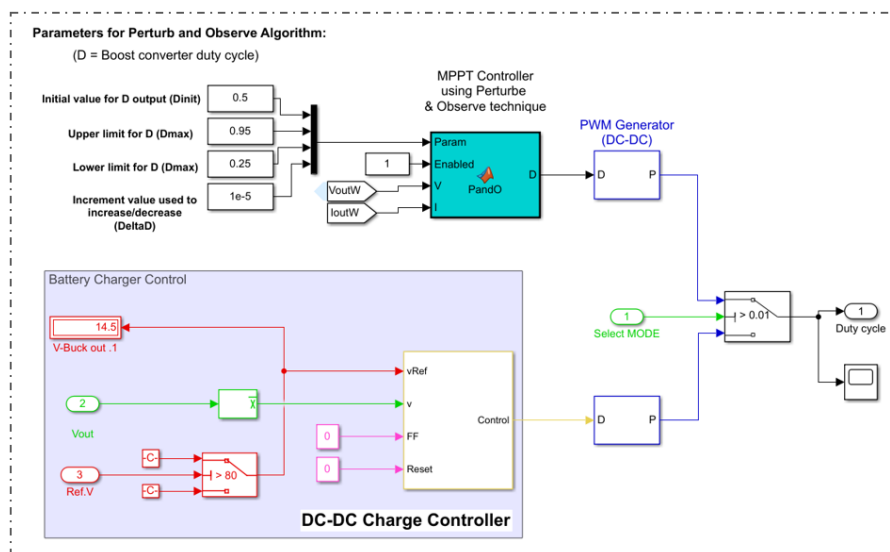


Figure 4.8: Battery charging model

4.5. Battery-Flywheel charge control method:

Flywheel storage systems have a high energy density, which allows them to be cycled frequently with less impact on performance. They are, therefore, suitable for applications requiring frequent cycling since they incur limited life reduction on excessive use. On the other hand, battery storage supports high energy loads but at low power. Therefore, our charging control methodology prioritizes battery charging and flywheel discharge. Figure 4.9 shows the control strategy for flywheel charging only when the battery state of charge (SOC) is above 80%. This ensures charging priority is given to the battery in the event of excess power output from the PV-Wind power generators.

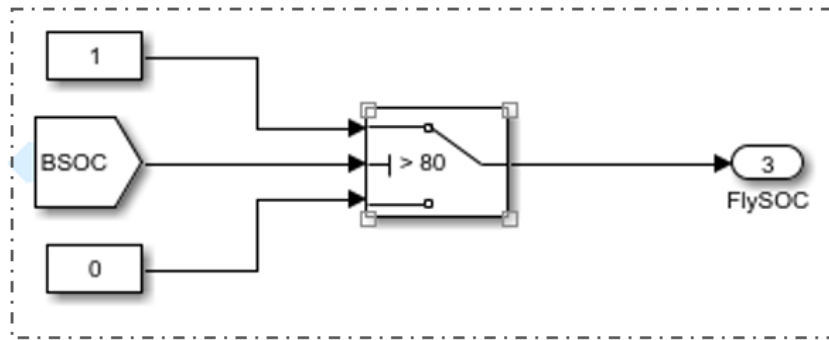


Figure 4.9: Flywheel-battery charge control scheme

4.6. Perturb & Observe Algorithm for MPPT Technique:

The perturb & observe maximum power point tracking (MPPT) algorithm is shown in Figure 4.10. This method calculates the power $P(t)$ by measuring the instant voltage $V(t)$ and current $I(t)$ and then compares it with last calculated power $P(t - 1)$. The algorithm continuously perturbs the system if the operating point is positive; otherwise, the direction of perturbation is changed if the operating point variation is positive. The DC/DC converter's duty cycle is varied until it reaches the maximum power point. To curb over-saturation, a limiter is placed at the output of PI controller, which is compared with the carrier signal to generate a pulse for the controlled switch IGBT of the DC/DC converter.

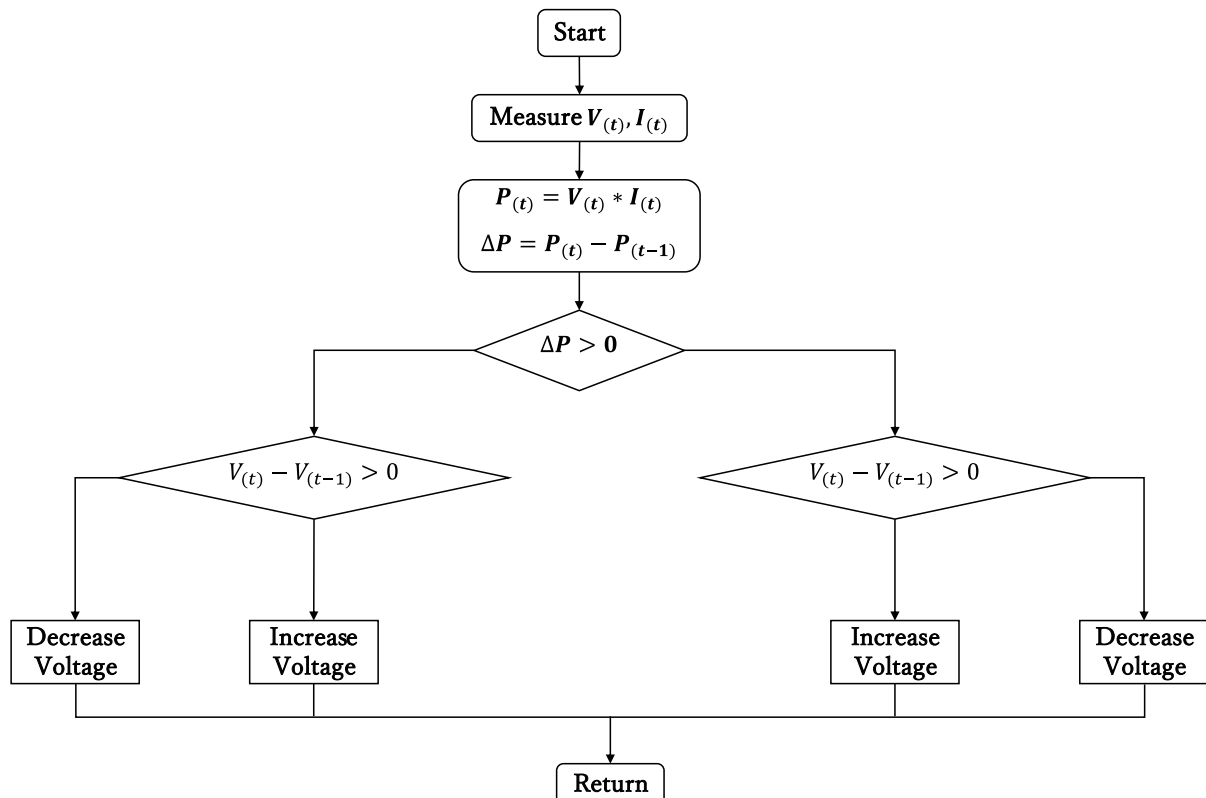


Figure 4.10: P & O MPPT algorithm flowchart

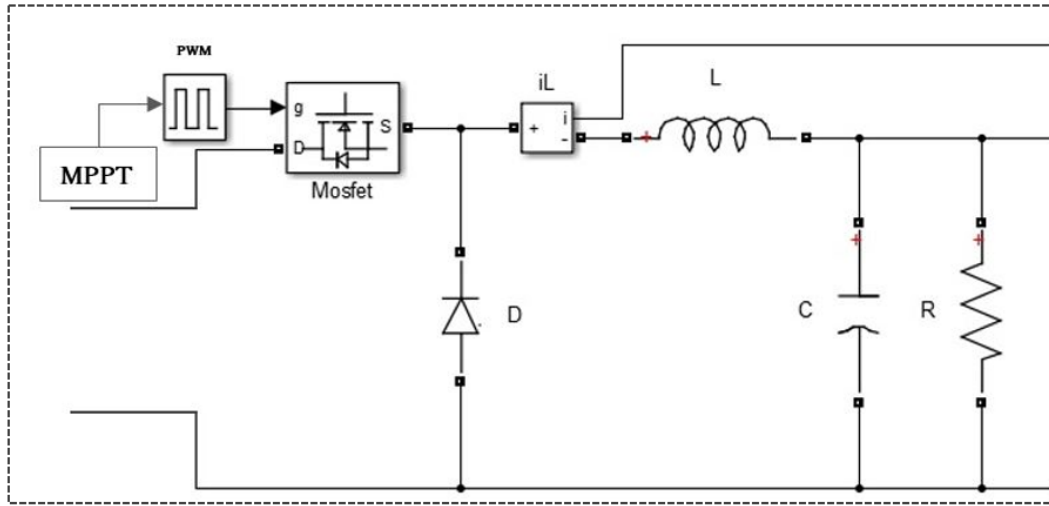


Figure 4.11: DC-DC buck converter control circuit

The buck converter operates by stepdown conversion of the applied dc input signal. The MOSFET or IGBT chopper circuit acts as a switch with a controlled switch, S . The inductor stores energy, ultimately delivering it to the load resistor. The power MOSFET or IGBT is turned off to maintain zero potential between the gate to the source terminal or to the collector terminal of the IGBT; the on-and-off variations result in a low-pass filter for the reduction in the output voltage (Jacob & Farzaneh, 2022). The low-pass LC filter is perfect for the generation of regulated dc output. The resistor, R , in the schematic DC-DC buck converter circuit in Figure 4.11, acts as a load to the circuit. The entire operation takes place in two separate modes. In the first mode, the switch is in a closed condition, thus allowing the current flow to occur. The inductor, L , in the current path stores energy in the form of a magnetic field. The capacitor also stores charge allowing voltage to appear across the load. According to Lenz's law, the energy stored in the inductor oppose the cause of its production, resulting reversal of polarity across the inductor due to induced current (Shaqour et al., 2020).

The total time, T combination is expressed in terms of T_{on} and T_{off} such that $T = T_{on} + T_{off}$ and the duty cycle is given by, $D = \frac{T_{on}}{T}$.

When the switch is closed, therefore the expression for the change in current becomes:

$$\Delta i_t = \left(\frac{V_{in} - V_0}{L} \right) T_{on} \quad (4-29)$$

In the second mode of operation, the switch is open, and the inductor acts as a source because it has stored energy. However, owing to reversed polarity by the inductor of the diode, D is in the forward-biased state. Therefore, the current is allowed to flow in the opposite direction until the inductor stored energy gets depleted. This makes the diode reverse-biased again, allowing the switch to be closed to start the cycle again automatically.

The current change rate through the inductor during the second mode of operation can be represented using the expression.

$$\Delta i_L = \left(\frac{V_0}{L} \right) (1 - D)T \quad (4-30)$$

The two modes represent a steady state operation with a recurring waveform, shown in Figure 4.12.

$$\int_0^T V_L dt = \int_0^{T_{on}} V_L dt + \int_{T_{on}}^T V_L dt = 0 \quad (4-31)$$

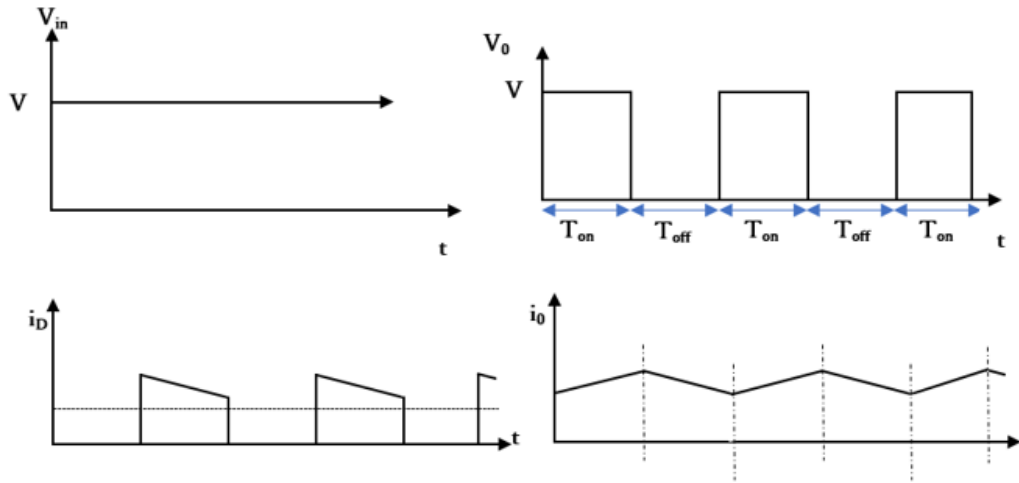


Figure 4.12: Buck converter operation waveforms

4.7. Input data used in the simulation:

The hourly wind speed input for the wind turbine generator and hourly radiations for the solar PV system input is shown in Figure A-1 and Figure A-2 respectively, while Figure A-3 represents the annual hourly temperatures in Makueni. The PV block has 13 parallel strings connected as two string pairs in series. The I-V and P-V characteristic curves for the PV system are demonstrated Figure 4.13 at $0^{\circ}C$, $25^{\circ}C$, and $45^{\circ}C$ cell temperatures. To stabilize the dc voltage from the PV system, $500\mu F$ DC link capacitor is connected in parallel.

The wind turbine is fed by wind speed, pitch angle, and generator speed. The turbine characteristics at $\beta = 0^{\circ}$ are shown in Figure 4.14. Output torque per unit is fed to the PMSG to generate three-phase AC voltage, which in turn its converted to DC voltage by the rectifier. A $500\mu F$ DC link capacitor is connected to the output.

A lithium-ion battery type of 12V/30Ah is used in this Simulink simulation. The initial state of charge is set at 60%. The lithium-ion battery is fully charged at 14.4V with a nominal discharge current of 2A and internal resistance of 0.014Ω . The parameter values for the HRES components are detailed in Table 4.1, Table 4.2, Table 4.3 and Table 4.4.

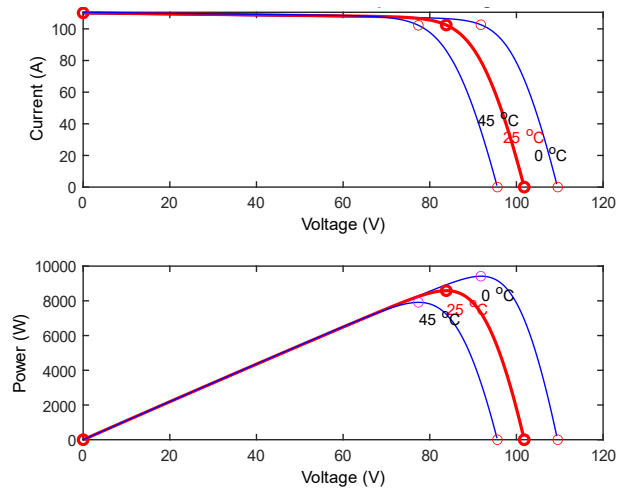


Figure 4.13: I-V and P-V curves

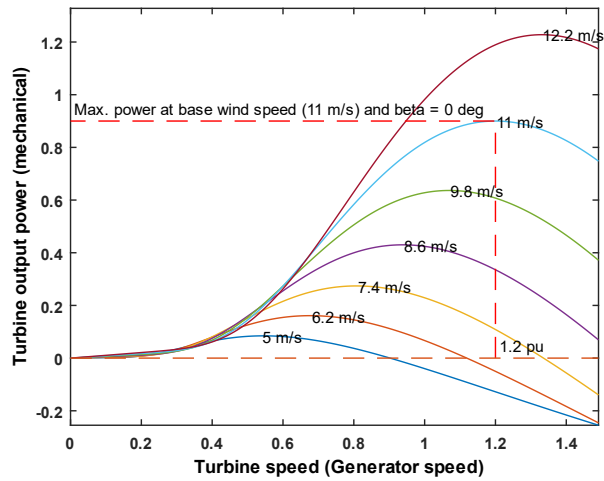


Figure 4.14: Turbine Characteristics at $\beta = 0^\circ$

Table 4.1: solar panel parameters

Parameters	Value
Rated power	330W
Peak voltage	41.9V
Open circuit voltage	50.9V
Peak current	7.88A
Short-circuit current	8.47A
Current temperature coefficient	-173.1mV/°C
Voltage temperature coefficient	3.6mA/°C
Number of cells N_s	83
Temperature range	-40°C to +85°C

Table 4.2: wind turbine parameters

Parameters	Value
Rated power	1kW
Rated voltage	110V
Startup wind speed	1.5m/s
Rated wind speed	10m/s
Maximum wind speed	50m/s
Rated rotation speed	300U/min
Fan blade quantity	3
Rotor blades diameter	2m
Tip speed	31m/s

Table 4.3: Battery parameters

Parameters	value
Type	Lithium-ion
Fully charge voltage	14V
20Hr Capacity	30AH
Charging current	2A-10A
Charging Voltage	14.4-14.9V
Float voltage	13.5-13.8V

Table 4.4: Flywheel parameters

Parameters	value
Flywheel poles	8
Inner radius	0.135m
Outer radius	0.15m
height	0.6m
Rotor mass	20kg
Mass density	760kg/m ³
Minimum rotation speed	1000rpm
Maximum rotation speed	9000rpm

Chapter 5

Results and Discussion

5.1 Area of study:

The annual data for the year 2021, solar radiation, ambient temperature, and wind speed, was collected from the Nguu area of Makueni county in Kenya, shown in Figure 5.1 (Climate.OneBuilding.Org, 2022). The electrical load profile was extracted from county government household energy consumption statistics and presented in Figure 5.2 (County, 2022). Using these data, different scenarios are optimized and verified to replicate an existing HRES power system.

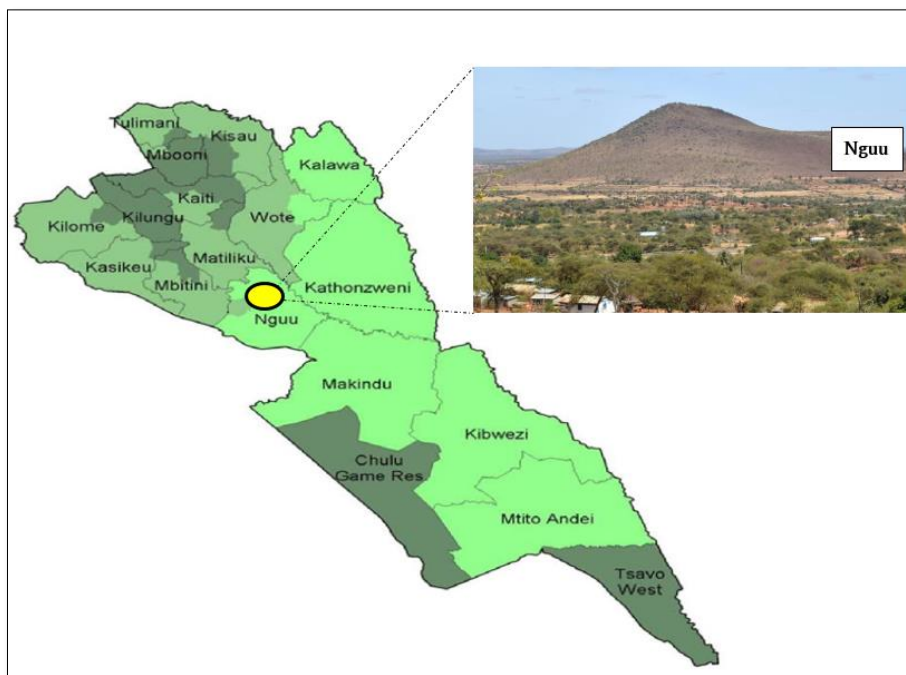


Figure 5.1: Schematic focus on the local area of research (Makueni, Nguu)

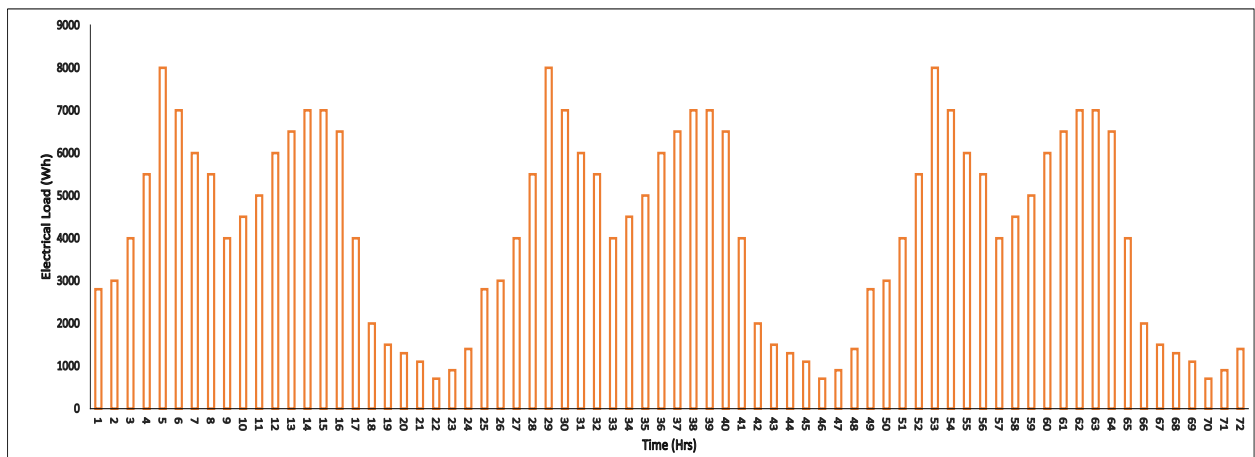


Figure 5.2: Hourly Electrical load profile for 72 hours in Makueni, Nguu.

5.2 Optimal design of the proposed HRES:

In Figure 5.3, an illustration of the multi-objective optimization Pareto front for the NLP ϵ -constraint solution in GAMS is demonstrated. The values of COE and UME for the f_1 and f_2 objective functions are tabulated for each hour of the year (8760 hours), giving a suitable compromise solution. This is because, a Pareto criterion exhibits a trading set-up in which neither side of the function merits without inversely affecting the other function. Therefore, this provides us with a course-effect experience on impacts associated with any decision; for instance, a reduction in energy cost leads to possible energy unreliability, and the reverse is true, as described in Figure 5.4. The iterations are looped for every hour of the year to produce a succession of optimum values for f_1 and f_2 appropriate in ensuring minimum cost of energy while avoiding possible blackouts in the HRES system. The value of the energy index of self-reliance, *EISR* is 0.9969 when the UME value is 0.00308, representing a strong reliability index according to equation (2-16). While the values of COE decrease, the values of *EISR* decrease, implying a reduced reliability state in the power supply if a lower cost of electricity is adopted.

The optimal results for the HRES system multi-objective optimization using the epsilon (ϵ)-constraint technique are summarized in Table 5.1. These results show a skewed dependence on the PV array as the most reliable form of power generation in comparison to the wind turbine. This situation can be accredited to a high level of radiation in the makueni area and the low capital and installation costs of solar PV systems. Battery storage is given more preference over flywheel; this also can be due to the high acquisition capital incurred in installing a flywheel storage system.

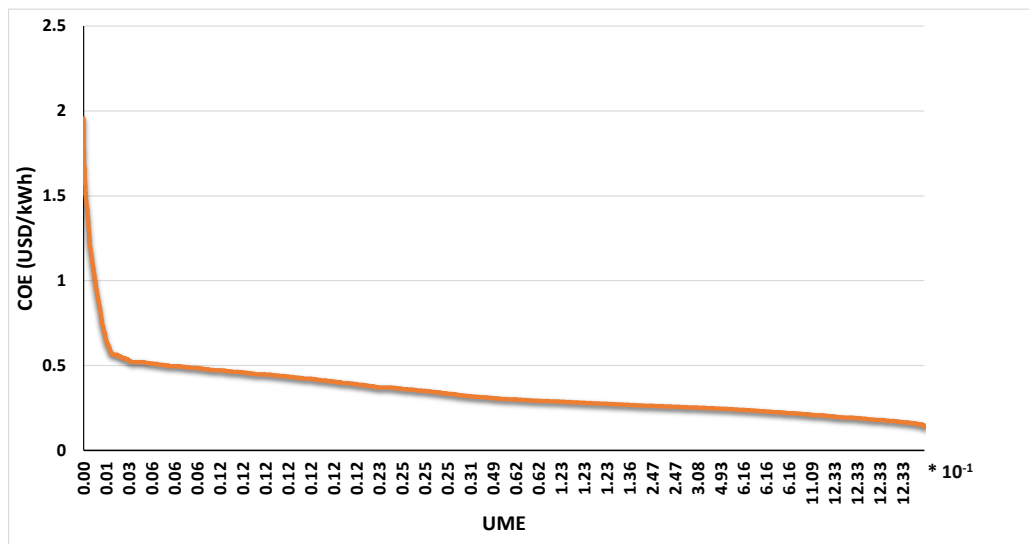


Figure 5.3: Pareto frontier for the multi-objective ϵ -constraint solution

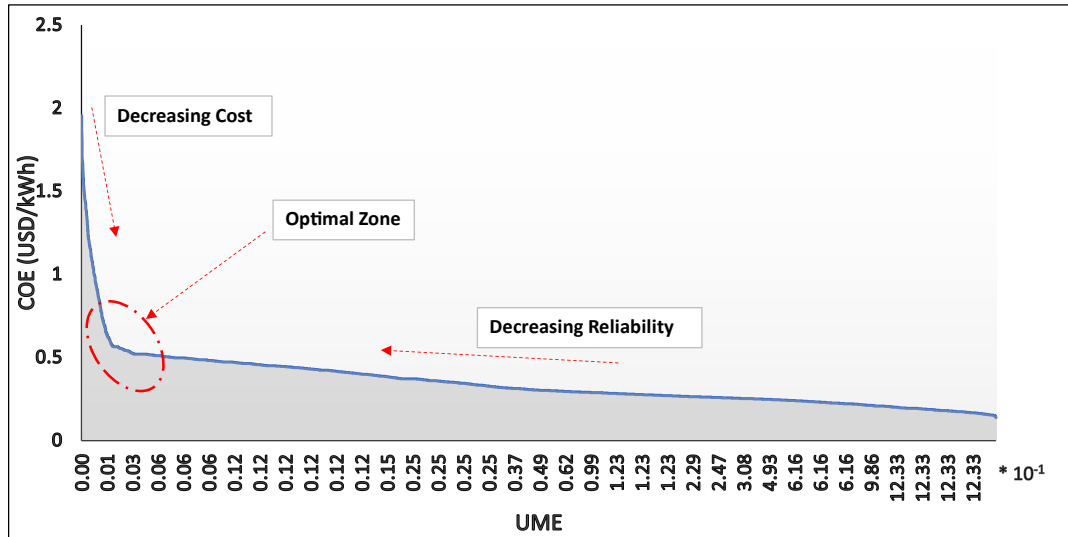


Figure 5.4: Pareto frontier for the multi-objective ϵ -constraint solution

Table 5.1: Optimization results

Output Variable	COE	UME	Number of PV modules(330Wp)	Wind Turbine (1kW Rating)	Battery Capacity (kWh)	Flywheel Capacity (kWh)
Optimal Value	0.519	0.003	26	3	22	4.7

5.3 Supply-demand balance during optimization

The five scenarios reported in Table 5.2 and optimized to effectively ascertain the ability of the HRES system to deliver reliable energy throughout different seasons in Kenya. The values obtained in these scenarios were visualized in Figure 5.5, Figure 5.6, Figure 5.7, Figure 5.8, and Figure 5.9 to illustrate optimal supply-demand balance in the different scenarios. It can be observed that, the hybrid storage of Battery/Flywheel (*HRESS*) effectively discharges to satisfy the demand during intermittence. Figure A-7 shows the annual energy supply – demand balance for the HRES system.

Table 5.2: Selected optimization scenarios

Scenario	Period	Season
I	February	warm/dry
II	April	long rain
III	June	cold/dry
IV	September	warm/dry
V	December	short rain

5.3.1 Scenario I:

The scenario results in Figure 5.5 were based on the meteorological conditions from the 10th day of February to the 12th day of February 2021, portrayed in Figure A-5 and Figure A-6. The area experienced a clear sky with long sunny hours recording high irradiance of up to 1330

W/m² peak values at 1300-1400 hrs on all days. The wind profile shows high speeds recorded throughout day one from 9hrs to 18hrs with a peak value of 8.2m/s. The supply–demand curve shows that electricity generation decreases from 850W at 0hrs to 109W at 4hrs, then gradually increasing to 9.2kW at 14hrs. the power output curve shows a decline until 185W at 45hrs. the electrical load profile is shown in Figure 5.2; this profile is adopted in all scenarios. Figure 5.5 demonstrates the HESS discharge from 0hrs to 10hrs to meet the load demand. At 10hrs, excess power is generated to reverse the HESS curve to charging. Generation is highest during the day and lowest at night when little or no radiation is received. The wind speed is lowest from 47hrs to 57hrs at 0.1m/s to 2.5m/s on the third day. The HESS discharge profile shows at 53hrs, a peak discharge of 8kW is attained to satisfy the peak demand on the third day of the scenario. Unpredictable variations in wind speed, as seen in Figure A-6, lead to heavy reliance on battery and flywheel storage systems.

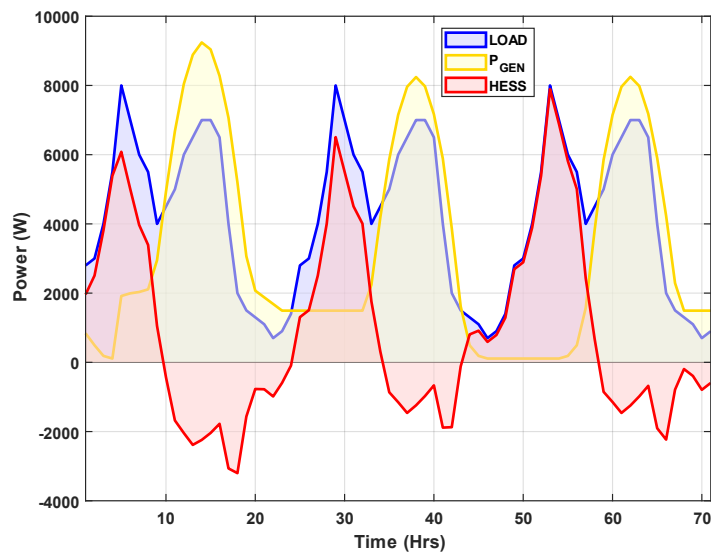


Figure 5.5: Energy supply-demand balance for Scenario I

5.3.2 Scenario II

Scenario II represents the long rain season extracted from the weather conditions from the 23rd to 25th days of April 2021, as illustrated in Figure A-5 and Figure A-6. The maximum irradiance reaches 1270W/m² between 13.00hrs – 14.00hrs for all three days. The average wind speed is 5.3m/s, and the maximum value is recorded at 7.2m/s. The energy balance scenario shown in Figure 5.6 depicts a similar power generation and HESS profile to scenario 1. However, in this scenario, since the load profile is similar, it can be observed that less power is generated to satisfy the load and charge the HESS. The maximum generation was attained at 7.8kW on 37hrs with a full charge capacity of 2.2kW on 41hrs and 65hrs. During the day, solar radiation is high; hence, high PV power is harvested. However, the area experiences unpredictable wind speed during these three days leading to low generation output at night hours and, thus, high discharge levels at night.

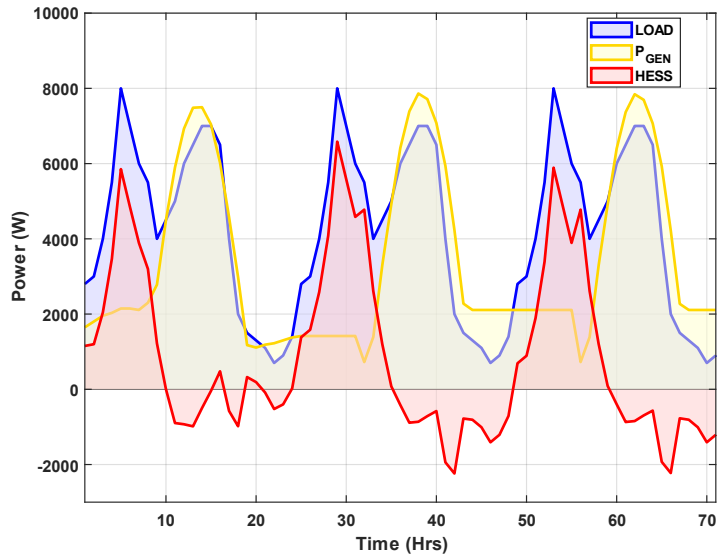


Figure 5.6: Energy supply-demand balance for Scenario II

5.3.3 Scenario III

The month of June 2021 is considered in scenario III. Weather data from 7/6/2021 to 9/6/2021 was acquired for this scenario, according to Figure A-5 and Figure A-6. This period represents the lowest levels of irradiance and wind speed. The average wind speed is 1.9m/s while the maximum irradiance is 790W/m² at 60hrs on the third day. The results in Figure 5.7 show that the HESS discharges from 0hrs to 66hrs when excess power is generated to charge the battery and flywheel storage.

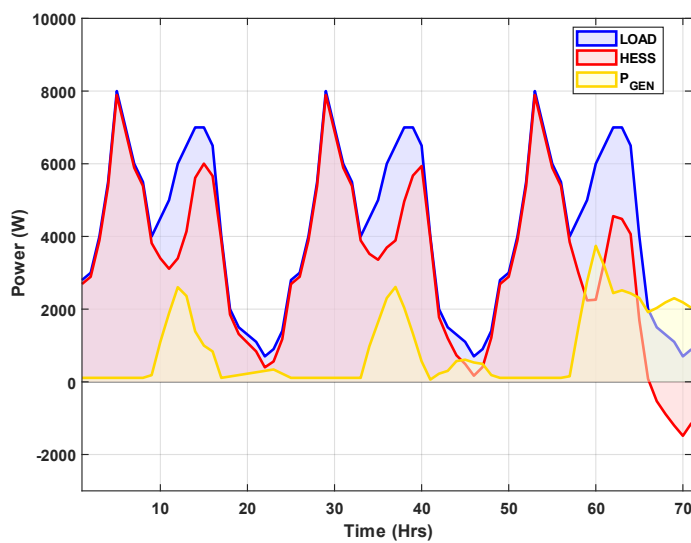


Figure 5.7: Energy supply-demand balance for Scenario III

5.3.4 Scenario IV

Figure 5.8 shows the energy balance obtained from diurnal optimization for meteorological conditions on the 14th to 16th days of September 2021. This month experiences the highest wind speed levels at solar irradiance, as indicated in Figure A-5 and Figure A-6. The maximum wind speed is 11.3m/s with an average of 6.2m/s. The days have a clear sky and high humidity with irradiance records of 1370W/m² at midday. The HRES supply-demand balance curve in Figure 5.8 shows during this scenario, the HESS discharges at 0hrs – 10hrs, 25hrs-34hrs, and 49hrs -58hrs. These profiles represent night hours when the system depends entirely on wind speed for a generation. The graph shows 3.4kW as the highest charge capacity attained at 61hrs on the third day. In this scenario, the maximum charge of the HESS is reached with less dependence on discharge due to favorable climatic conditions.

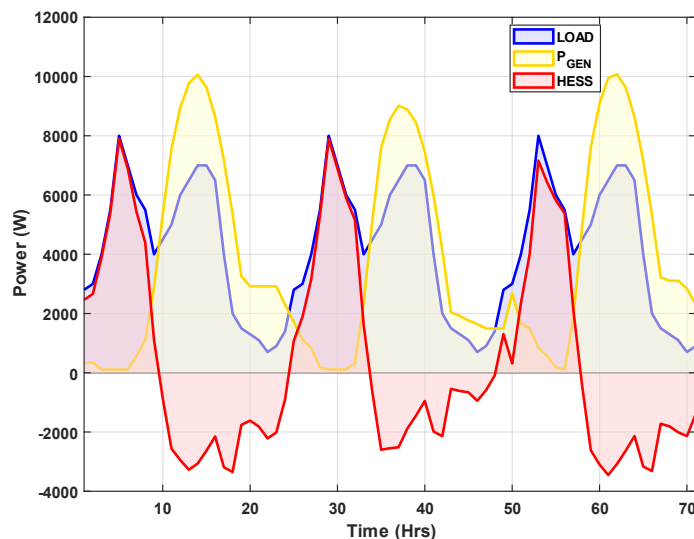


Figure 5.8: Energy supply-demand balance for the Scenario IV

5.3.5 Scenario V

The daily conditions for scenario V are represented in Figure A-5 and Figure A-6. These illustrations show peak irradiance received during the midday hours of the 20th and 22nd days of December 2021 at 1330W/m². The wind speed average for this scenario is 2.4m/s, with several hours of the three days recording 0m/s wind speed levels. Figure 5.9 represents the results of optimization for this scenario. According to the results, the system relies on HESS to satisfy the electrical demand at 0hrs to 10hrs, 25hrs to 34hrs, and 49hrs to 58hrs. This is accredited to low solar radiation during these hours and high negative variation in wind speed.

From these scenarios, it can be observed that the system is highly reliable, meeting the load demand sufficiently in all meteorological conditions experienced in the area of study. On top of this, Figure A-7 shows an annual supply-demand balance curve for 2021, depicting

100% satisfaction of the electrical load from PV-wind power generation and battery-flywheel discharge.

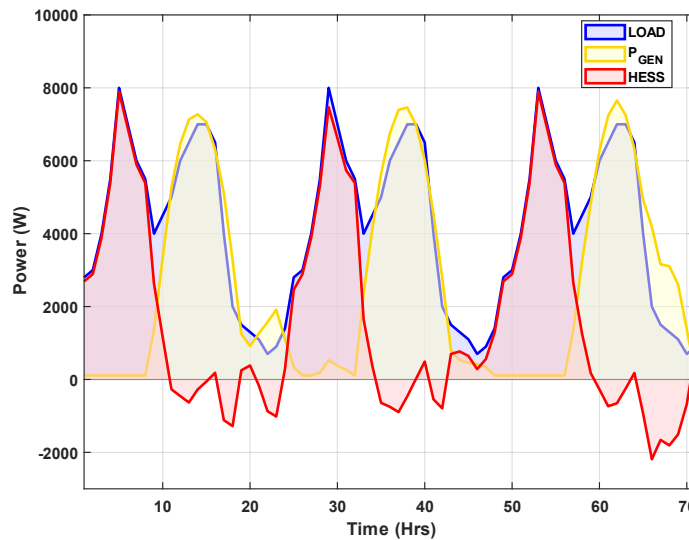


Figure 5.9: Energy supply-demand balance for the Scenario V

5.4 HRES dynamic operation and simulation:

The estimated optimal size of the components reported in Table 5.1 was used in the Simulink model in order to evaluate the hourly performance of the proposed HRES under different operating conditions. The PV module consists of 26 PV modules connected in series, each rated 330Wp. This sums to a theoretical maximum power output of 8.58 kWp. Three wind turbines rated at 1kW and operating at a rated speed of 10m/s are utilized in the model. A storage bank made-up of a lithium-ion battery is implemented at a capacity of 30Ah, 12V offering high-efficiency storage benefits. In addition, an 8-pole, PMSM-based flywheel with a maximum speed of 9,000 rpm and 4.7kWh storage capacity is modeled in the HRES system to augment the battery storage. Table 4.1, Table 4.2, Table 4.3, and Table 4.4 detail the parameter size for the HRES components used in the Matlab Simulink simulation.

According to the illustrated area of study in Figure 5.1, the off-grid HRES system is proposed to supply power steadfastly to 300 households, two schools, a community health center, and a small shopping center with a population of 200 – 250 people during the daytime and 100-150 people during the night. Using Ohm’s law, the power load demand for the community as shown in Figure 5.2, is converted to a dynamic resistive load in the Matlab-Simulink model for 72 hours of operation. The wind speed, irradiance, and solar cell temperature for three simulation days are extracted from actual data visualized in Figure A-1, Figure A-2 , and Figure A-3, respectively. These inputs are represented in Figure 5.10 and Figure 5.11 for the 72-hour operation in Simulink.

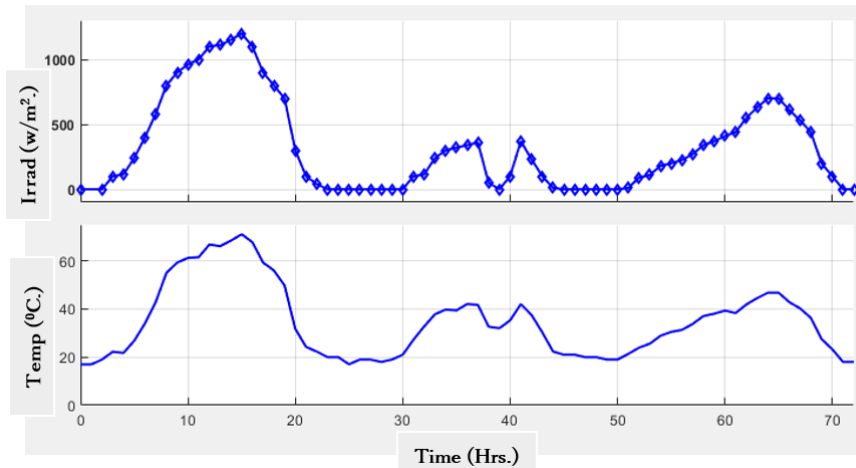


Figure 5.10: Irradiance (w/m²) and cell temperature (°C)

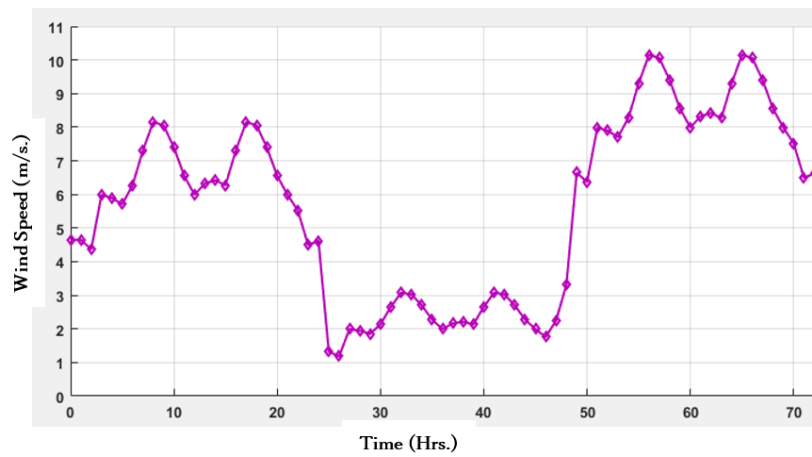


Figure 5.11: Wind Speed in m/s

The simulation results in Figure 5. 12 illustrate the operation output for the HRES system for an arbitrary 72-hour scenario weather condition in Makueni during the month of June 2021. Climatic data in June is preferred because Makueni experiences low radiation and wind speeds during this time of the year. The system results visualization shows an effective power balance and perfect complementation between the electrical load demand and power generation and between charging and discharging operations based on the given optimal size of the HRES. The battery and flywheel charging are highlighted in this figure by a curve of negative gradient, while the discharge state is represented using positive gradient points. A P&O MPPT charge controller is used to ensure the extraction of maximum power from PV and wind turbine performance by forcing maximum power point operation at fluctuating irradiance and wind speeds. The system is feasibly reliable since the model sustainably stores excess power and discharges accordingly to supplement higher loads at night and during intermittency hours.

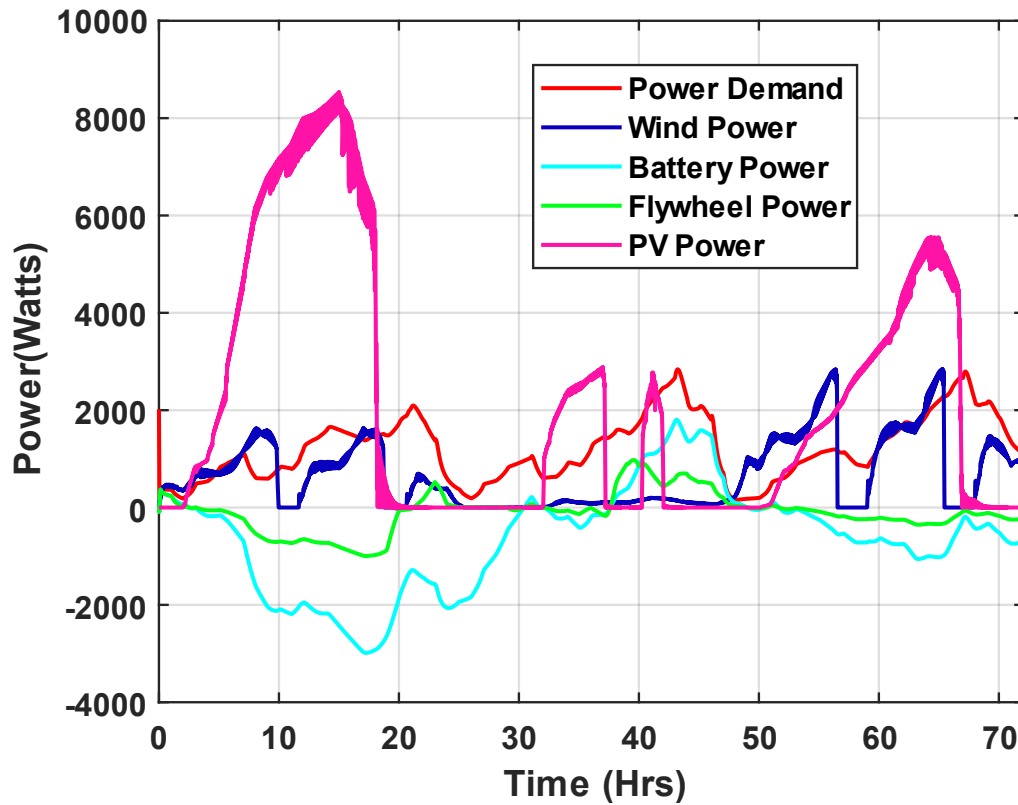


Figure 5. 12: Overall system performance for 72 hours of operation of the proposed HRES

5.4.1. FESS frequency response advantage:

Islanded microgrids have a major challenge of supply-demand uncertainties leading to low system inertia with possible varying frequencies. Such a state may expose the system to a complete blackout if measures are not implemented to balance supply with load demand. Diesel generators can play a critical role as a reserve, providing backup power to balance the load demand, though this option is considered detrimental due to the CO₂ emissions of diesel generators. In this research, the flywheel energy storage system (FESS) alleviates possible blackouts due to frequency-based power imbalance. Based on the operation profile shown in Figure 5. 12, FESS is charged with positive torque generated upon excess power from the combined solar/wind output, wind power system, or PV power system. At any given moment, the flywheel charging lags the battery charge curve because the charge control prioritizes battery charging. When the demand exceeds the total PV/Wind power output, the flywheel reverse-spins fast to respond to the abrupt deficit to satisfy the power deficiency in the HRES system. This is demonstrated in magnified sections of Figure 5.13; the battery response here lags the flywheel, whose discharge curve, in comparison, tends positive promptly. This effectively substantiates the significance of the flywheel as an ideal spinning reserve for balancing the supply with electrical load demand.

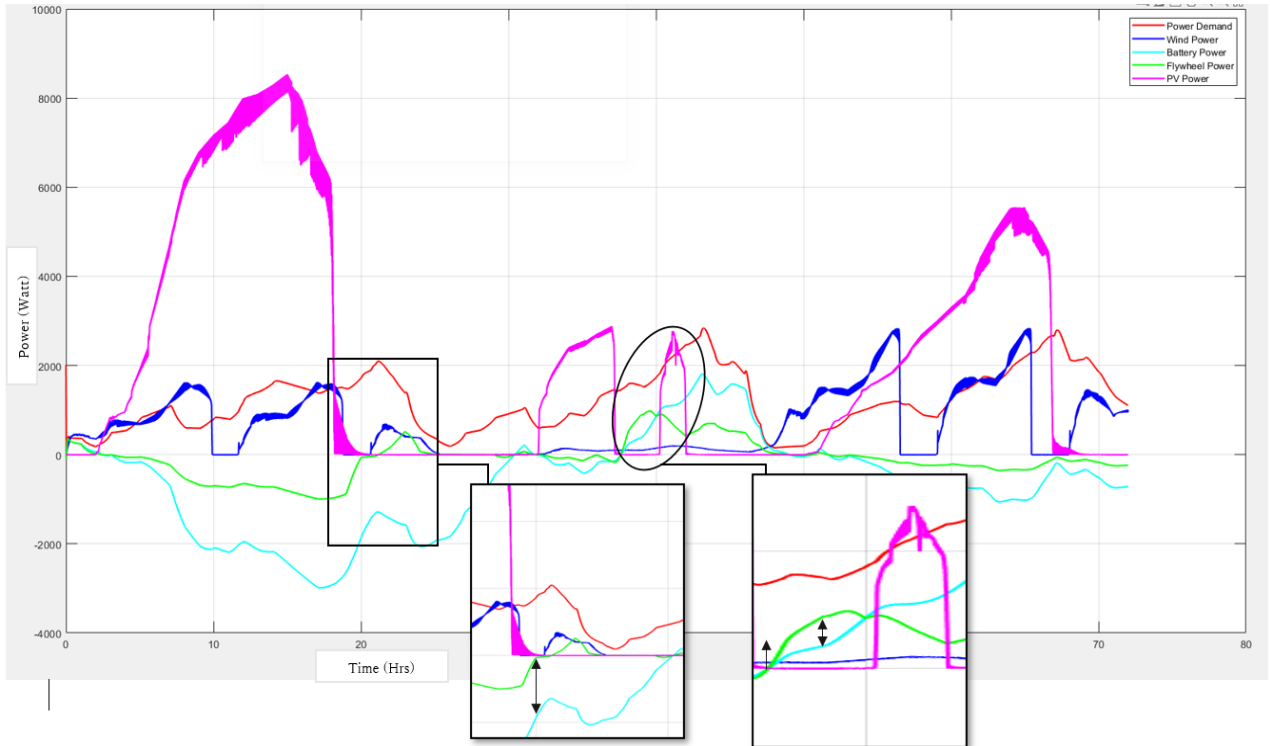


Figure 5.13: Flywheel-Battery system response to load demand at low solar/wind power generation

5.4.2 Battery capacity gain:

Using a flywheel in this HRES system further increases the battery storage capacity by a factor of 0.00886% every 72 hours of operation, as demonstrated in Figure 5.14 and Figure 5.15. The graphs illustrate how the state of charge, SOC and, depth of discharge, DOD of the battery energy storage system (BESS) are affected by the flywheel operation in the system. The SOC and DOD are the major factors for determining the number of cycles of a battery within a given period of operation. This consequently underlines the aging characteristics of a battery system which ultimately dictates the lifespan and cost of storage systems. Figure 5.15 represents a state of charge curve for the battery storage with and without a flywheel. In this case, the SOC of the battery with the flywheel maintains a higher charge percentage compared to when the flywheel is not running. The most important observation here is how the loss of charge is minimal when hybridized storage (BESS/FESS) is used, contrary to SOC with stand-alone battery storage. Figure 5.14 compares the DOD of the system with and without a flywheel storage system (FESS). The graph demonstrates a slowed discharge for hybrid Battery/Flywheel storage of 0.00886% for 72 hours of operation. This is equivalent to a 7045Wh storage capacity gain in 72 hours of HRES operation and an 858kWh capacity increment for one year, as exemplified in Figure 5.16. The use of the flywheel, therefore, provides an effective degradation mitigation system in which a substantial improvement in the life cycle and capacity of the battery is attained.

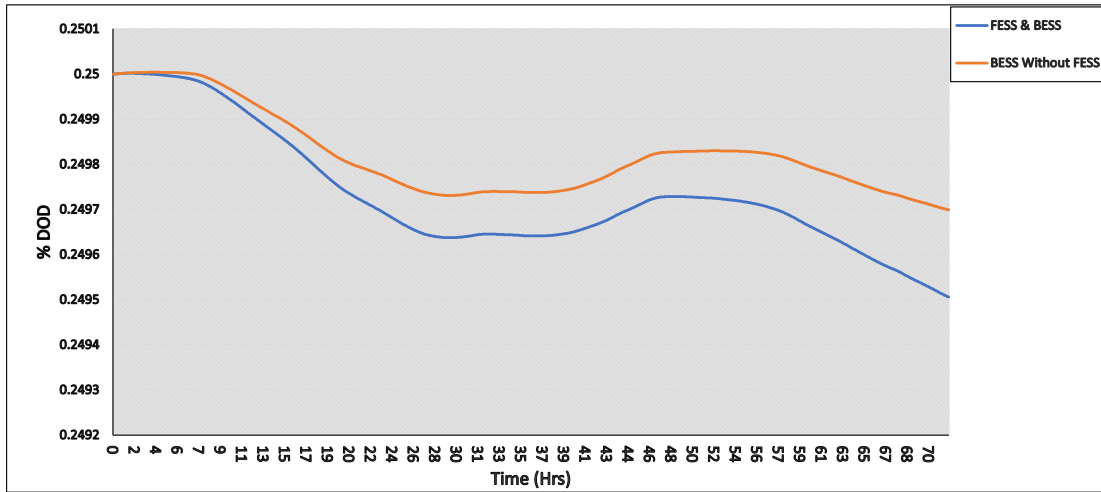


Figure 5.14: A comparison of the system's DOD with and without the FESS

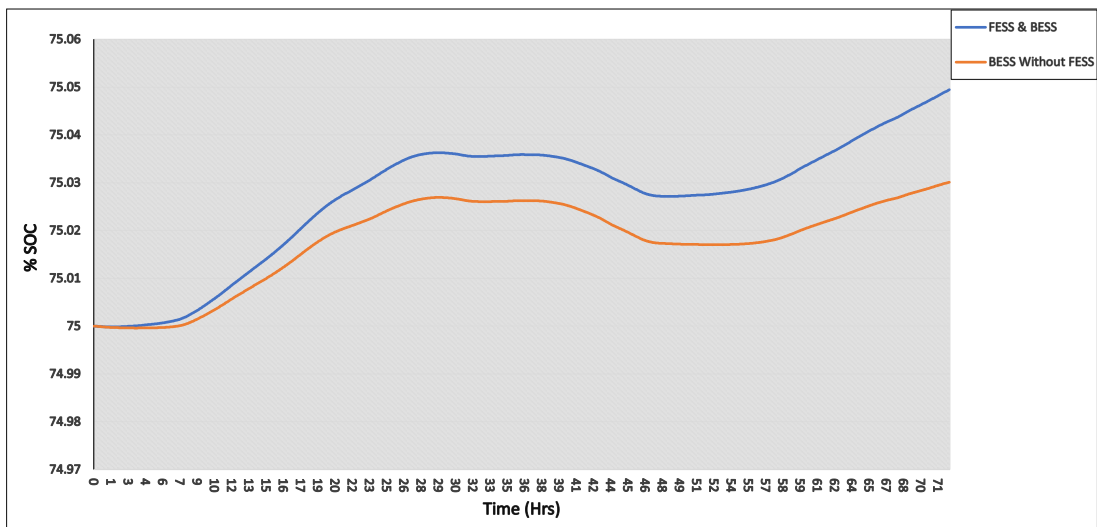


Figure 5.15: State of charge (SOC) for the battery with and without the flywheel

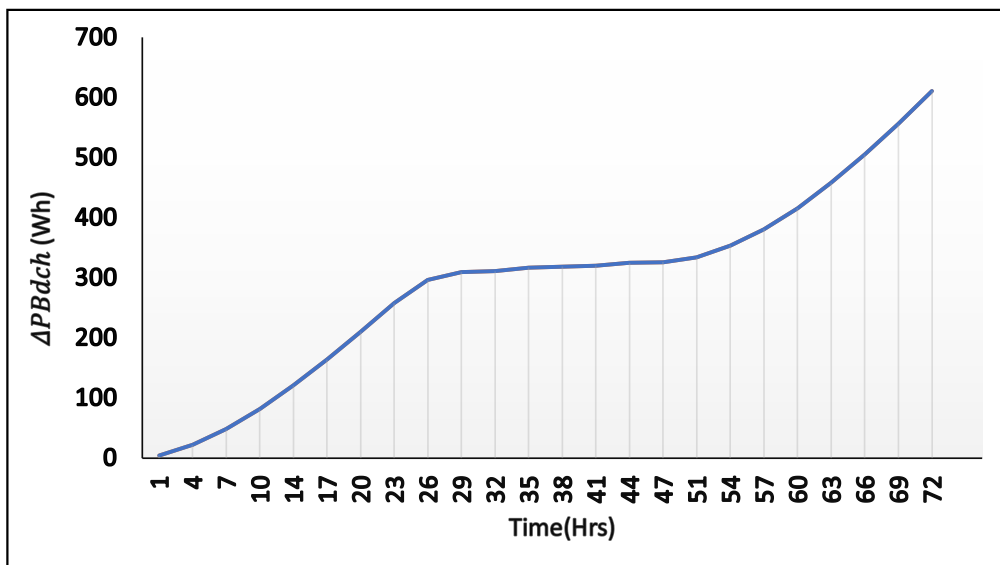


Figure 5.16: Battery capacity gain with battery/flywheel storage system

Chapter 6

Conclusion

This research introduced a comprehensive modeling approach to find the optimal size, configuration, and operation of the proposed PV-Wind-Battery-Flywheel HRES, to be used as an off-grid microgrid in remote areas in Kenya. Developing countries like Kenya and other sub-Saharan African countries require stand-alone microgrid systems to provide electricity in remote areas. However, a few considerations limit the choice of implementation of such microgrids: owing to the low-income status of residents in these regions, the cost of electricity must be affordable. Furthermore, most of these remote zones are entirely isolated from the grid system and consequently need highly reliable power supply systems. Moreover, the necessity to reduce the use of fossil fuel-based power generators, which emit greenhouse gases, further justifies the need to exploit effective and efficient storage technologies in implementing clean energy microgrid systems.

This research recommends employing PV-wind-battery-flywheel microgrid stand-alone systems for Kenya's isolated rural areas because of the following reasons demonstrated in this study: low cost of electricity and high reliability due to efficiency in control and complementation during power generation and storage. An efficient and dependable hybridized storage system cushions the micro-grid system from possible power shutdown. Low cost of maintenance characterized by zero greenhouse gas emissions and reliance on natural renewable sources plentifully available in Kenya. In addition, this microgrid system allows for expansion in both generation and storage components to cater to expanded electrical loads. This enables the government to adopt a phased implementation strategy in actualizing the HRES power system.

To this aim, the optimal sizing model was founded on a multi-objective function optimization, considering both LCOE and reliability as the objective function. Using an applicable energy index, EISR, as a measurement tool in visualizing the relationship between the COE and the UME, a Pareto front was generated in which the optimal configuration of the system at the minimum cost and maximum reliability of the system can be found. In addition, a dynamic power control simulation model was developed in Matlab-Simulink in order to evaluate the hourly power supply demand of the HRES under different operating conditions.

The multi-objective optimization results for COE were realized at 0.519 USD/kWh depicting a suitable compromise for high-reliability levels and electricity affordability. The value of unmet energy, UME, was found at 0.00308, showing that HRES can supply electricity consistently. These results demonstrate the efficiency of the off-grid HRES system installed in a remote area with an annual electricity demand of 37.94MWh. The ability of the system to utilize 26 solar PV panels, 3 wind turbines, and a HESS system made up of battery and flywheel to gain high reliability at affordable COE illustrates a commendable need to incline on renewable energy systems. The optimal storage capacity for the battery and flywheel, 22kWh and 4.7kWh, respectively, represent the need for storage to achieve energy reliability.

The simulation results on Matlab/Simulink demonstrate the adequate performance of the proposed HRES. The PV and wind turbine systems are both linked to the electric load and the storage system. The MPPT efficiently tracks the maximum power point of the PV array discussed earlier. The charge and discharge control for the battery and the flywheel provides a multi-faced benefit: the advantage in frequency response and the gain in battery capacity. The FESS demonstrates a fast frequency response in the event of a sudden halt in power generation by the PV and wind turbine systems. Such conditions, where no radiation and wind speeds are very low, lead to an unexpected overreliance on the storage system. As demonstrated and discussed in this study, the flywheel storage system provides a fast dynamic response and high energy density necessary to avoid possible power outages. A comparison and analysis of battery storage capacity behavior both with and without hybrid storage in the HRES system shows a significant increment in capacity when the BESS-FESS storage system is assumed. This increase in battery capacity is because of mutual complementation in the ESS. The battery retains substantial charge, which helps reduce the possible number of cycles and hence increases battery storage capacity.

Appendix

Table A-1: Recommended average days for months and values of **n** by months (Duffie et al., 1985)

Month	n for i^{th}	For Average Day of Month	
	Day of Month	Date	n
January	i	17	17
February	31+i	16	47
March	59+ i	16	75
April	90+ i	15	105
May	120+ i	15	135
June	151+ i	11	162
July	181+ i	17	198
August	212+ i	16	228
September	243+ i	15	258
October	273+ i	15	288
November	304+ i	14	318
December	334+ i	10	344

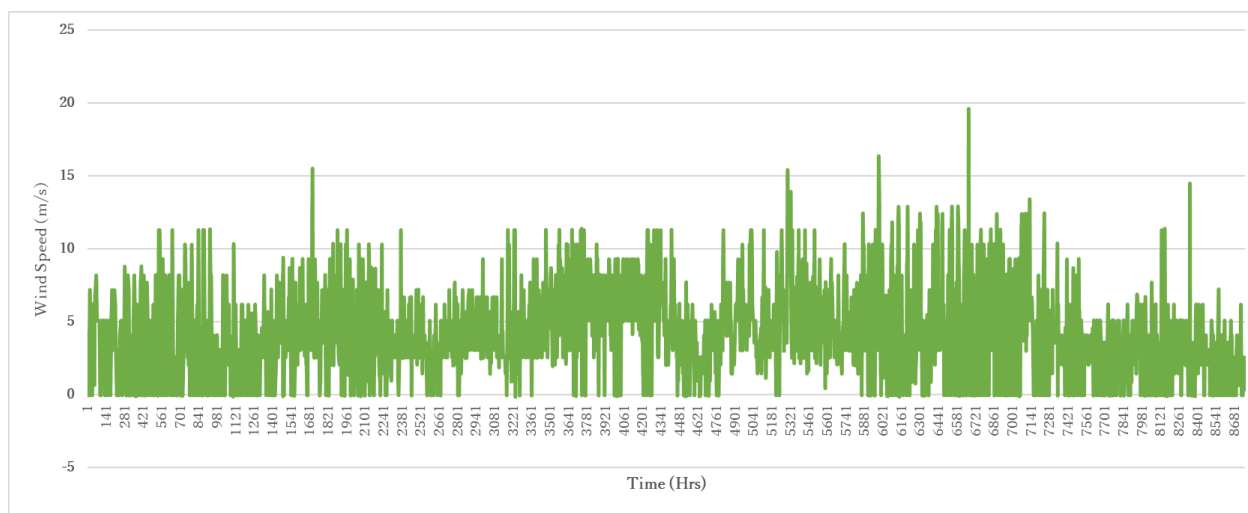


Figure A-1: Annual hourly wind speeds in the Makueni area for 2021

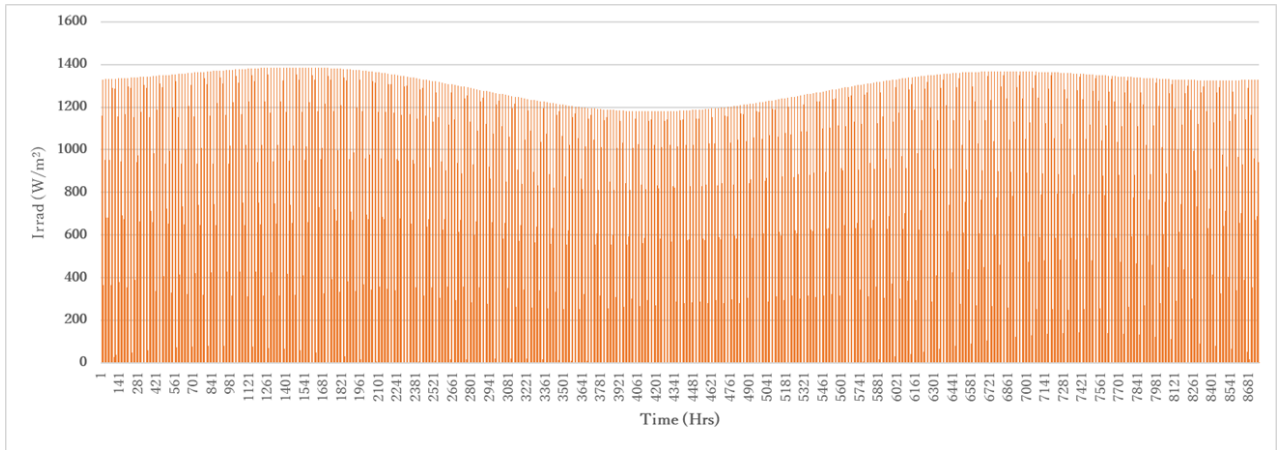


Figure A-2: Annual hourly irradiance in Makueni for 2021

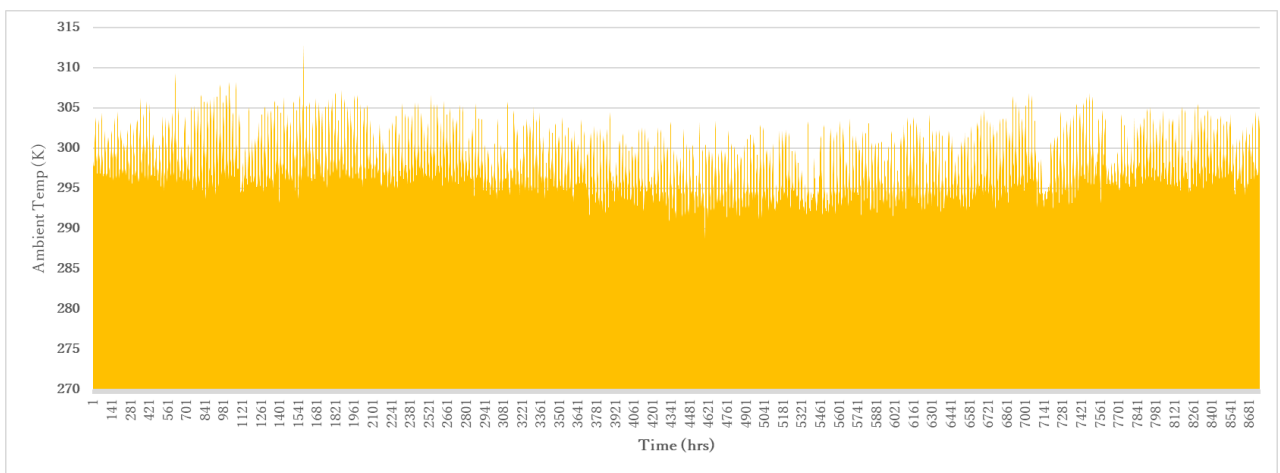


Figure A-3: Annual hourly ambient temperatures in Makueni area for 2021

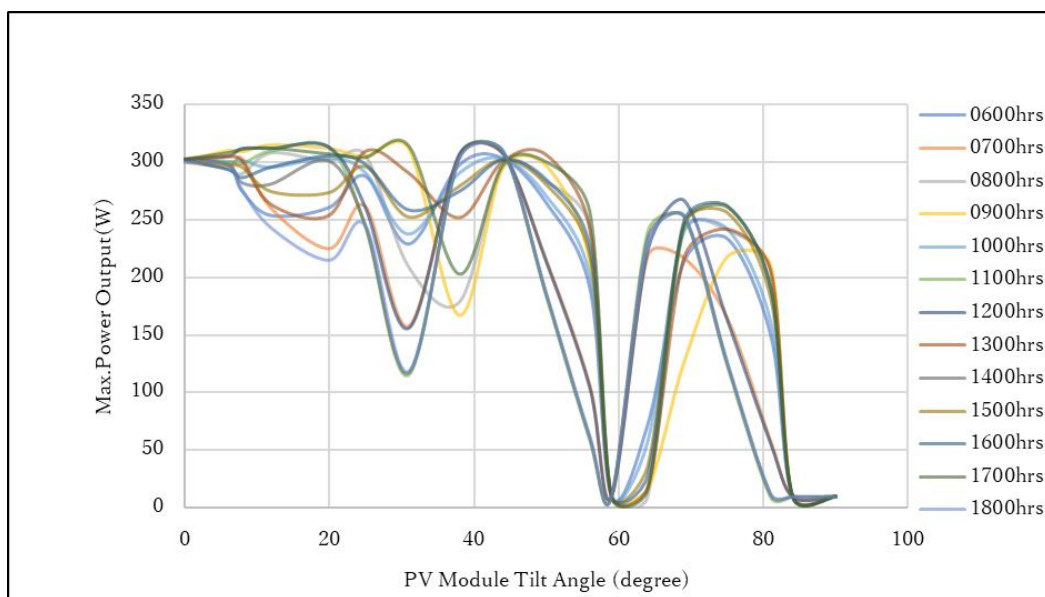


Figure A-4: Tilt angle vs. power output variations for a 330Wp PV panel in 12 hours

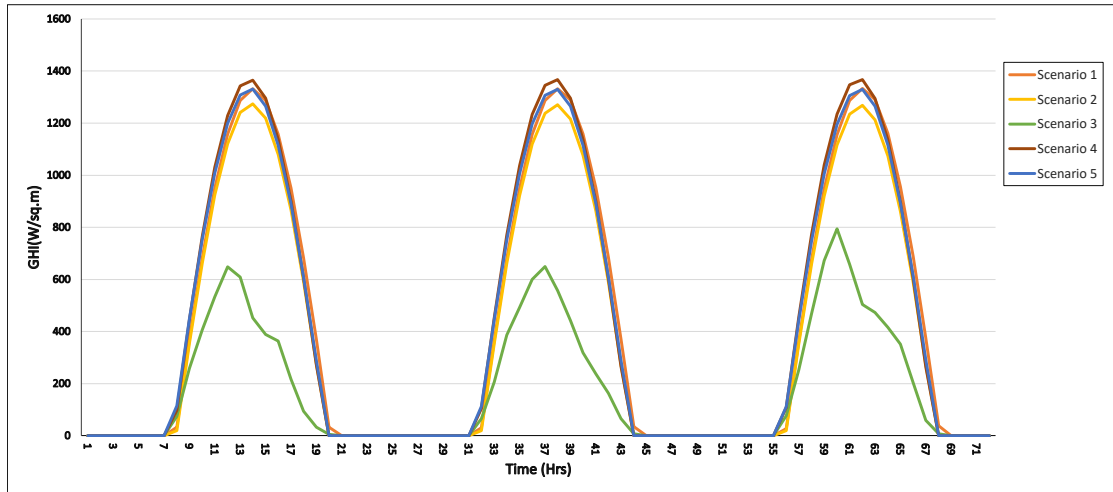


Figure A-5: Radiation for the different scenarios

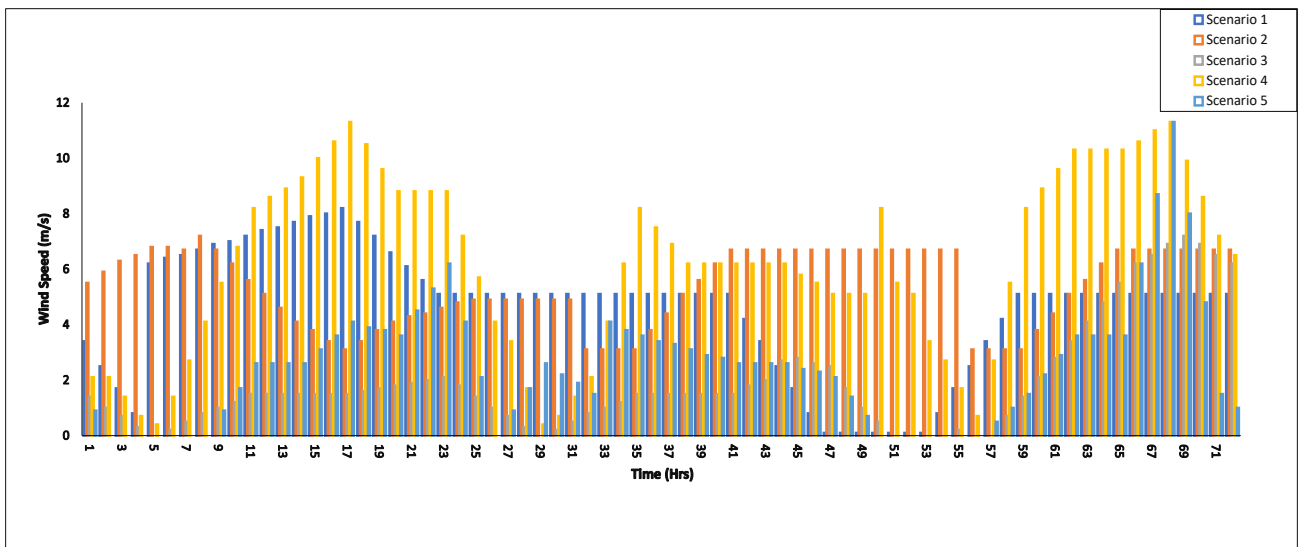


Figure A-6: Wind speed for different scenarios

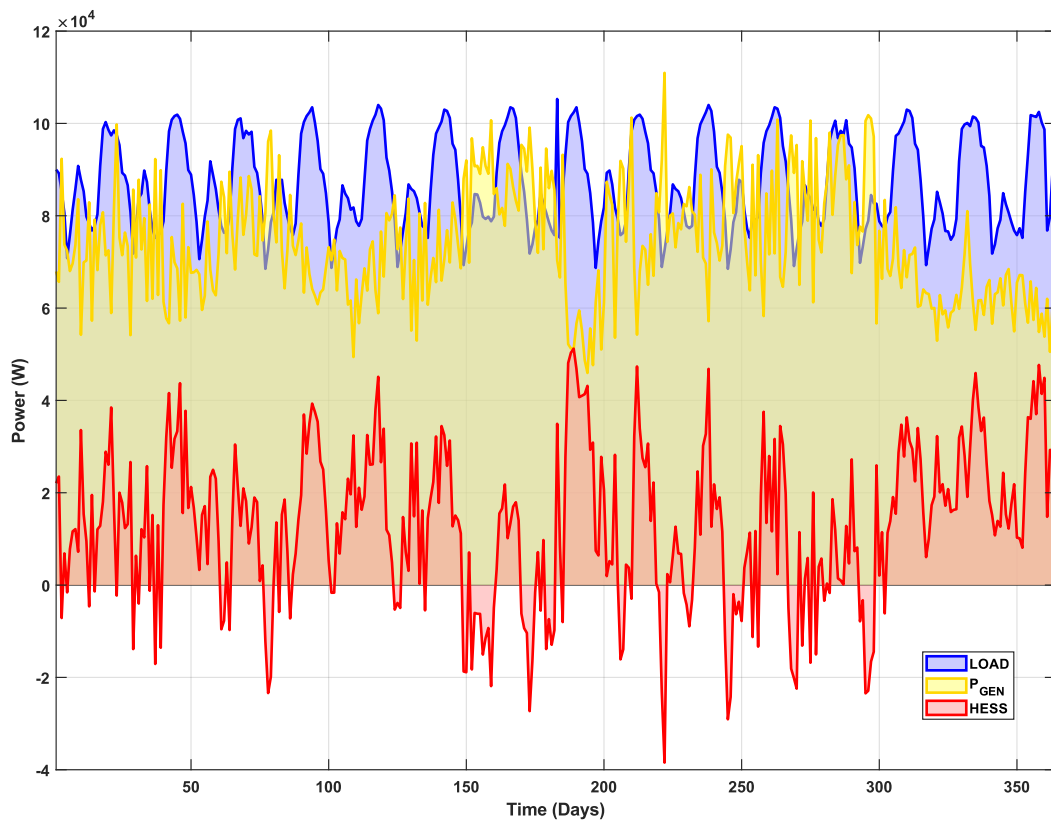


Figure A-7: Annual energy supply-demand balance for 2021

Nomenclature

<i>HRES</i>	Hybrid Renewable Energy System
<i>COE</i>	Cost of Energy
<i>EISR</i>	Energy Index of Self Reliance
<i>SSA</i>	Sub-Saharan Africa
<i>SDG</i>	Sustainable Development Goals
<i>GAMS</i>	General Algebraic Modelling System
<i>FESS</i>	Flywheel Energy Storage System
<i>BESS</i>	Battery Energy Storage System
<i>HESS</i>	Hybrid Energy Storage System
<i>EPRA</i>	Energy and Petroleum Regulatory Authority
<i>IRENA</i>	International Renewable Energy Agency
<i>DC</i>	Direct Current
CO_2	Carbon dioxide
P_{Gen}	Power generated
<i>UME</i>	Unmet Energy
<i>RES</i>	Renewable Energy Sources
<i>MOPSO</i>	Multi-objective Particle Swarm Optimization
<i>LPSP</i>	Loss of Power Supply Probability
<i>DG</i>	Diesel/fossil Generators
<i>AC</i>	Alternating Current
<i>PMSG</i>	Permanent Magnet Synchronous Generator
<i>PMSM</i>	Permanent Magnet Synchronous Machine
<i>SVPWM</i>	Space Vector Pulse Width Modulation
<i>MPPT</i>	Maximum Power Point Tracking
<i>DNI</i>	Direct Normal Incident
<i>DHI</i>	Diffuse Horizontal Incident
<i>GHI</i>	Global Horizontal Incident
<i>P&O</i>	Perturb & Observe
<i>LCOE</i>	Levelized Cost of Electricity
<i>PI Controller</i>	Proportional Integral Controller
OMC_i	Annual Operation and Maintenance Cost
RC_i	Replacement Cost
f_1	Objective function for COE
f_2	Objective function for <i>UME</i>
<i>r</i>	Discount Rate
<i>y</i>	Total component Lifespan
<i>i</i>	Number of Component Type
<i>PBdch</i>	Battery power discharge
<i>PFWdch</i>	Flywheel power discharge
α	Solar PV panel tilt angle

γ	Surface azimuth angle
φ	Solar azimuth angle
β	Solar altitude angle
l	local latitude
h	hour angle
δ	Solar declination angle
T	Solar time
EOT	Equation of time
I_T	Total insolation
T_c	Cell temperature
T_a	Ambient temperature
$NOCT$	Nominal operating cell temperature
STC	Standard test conditions
G_g	Insolation at T_a
G_o	Insolation at NOCT
P_{pv}	PV power output
G_{pv}	Nominal PV power output at STC
I_D	Diode current (A)
I_L	Photocurrent (A)
I_{mp}	Current at Maximum Power Point (A)
I_{sc}	Short circuit current (A)
a	Modified diode ideality factor
n	Diode ideality factor
N_s	Number of PV cells
R_s	Series resistance (Ω)
R_p	Shunt resistance (Ω)
h_{hub}	Turbine height
h_{ref}	Reference turbine height
v_{ref}	Wind Speed at reference height
p_{rated}	Rated turbine power
v_{rated}	Rated turbine wind speed
v_{cut_in}	Minimum turbine wind speed
v_{cut_out}	Maximum turbine wind speed
P_{WT}	Power generated by the wind turbine
I	PV Output current (A)
I_o	Diode saturation current (A)
V	Terminal PV voltage (V)
V_{mp}	Voltage at Maximum Power Point (V)
V_{oc}	Open circuit voltage (V)
V_w	Wind speed (m/s)
w_f	Rotor angular velocity(rad/s)
C_p	Turbine power coefficient

ρ	Air density (kg/m ³)
A	Turbine swept area (m ²)
u	Wind speed (m/s)
λ	Tip speed ratio of the wind turbine
β	Blade pitch
r_m	Turbine rotor radius
w_r	Angular velocity of turbine (rad/s)
V_{sd}, V_{sq}	Stator circuit voltages
R_s	Stator winding resistance
I_{sd}, I_{sq}	Stator circuit currents
d, q	Stator reference frames
ω_m	Rotational speed
ψ_{sd}, ψ_{sq}	Flux linkages
L_{sd}, L_{sq}	Leakage inductances
L_{md}, L_{mq}	Magnetizing inductances
ψ_m	Linkage flux
J	Load combined inertia
F	Combined viscous friction
T_f	Shaft static friction
T_m	Mechanical torque
θ	Angular position
E_{FW}	Kinetic energy stored by flywheel
I	Flywheel moment of inertia
r_o, r_i	Flywheel radius (outer & inner)
w_f	Flywheel angular velocity
SOC	State of Charge (%)
DOD	Depth of discharge
$P_{bat-discharge}$	Battery discharge power
$P_{FW-discharge}$	Flywheel discharge power
λ_{sys}	System failure rate
ε	Random value, epsilon
E_{bat}	Energy storage by battery
E_{gen}	Electrical energy generated
E_L	Electrical load
I_{bat}	Battery charging current

References

- Akbari, A., Vahidinasab, V., Arasteh, H., & Kazemi-Robati, E. (2022). Rural and residential microgrids: concepts, status quo, model, and application. *Residential Microgrids and Rural Electrifications*, 131–161. <https://doi.org/10.1016/B978-0-323-90177-2.00007-4>
- Akhavan Shams, S., & Ahmadi, R. (2021). Dynamic optimization of solar-wind hybrid system connected to electrical battery or hydrogen as an energy storage system. *International Journal of Energy Research*, 45(7), 10630–10654. <https://doi.org/10.1002/ER.6549>
- Al-Shereiqi, A., Al-Hinai, A., Albadi, M., & Al-Abri, R. (2021). Optimal Sizing of Hybrid Wind-Solar Power Systems to Suppress Output Fluctuation. *Energies 2021, Vol. 14, Page 5377*, 14(17), 5377. <https://doi.org/10.3390/EN14175377>
- Alberizzi, J. C., Frigola, J. M., Rossi, M., & Renzi, M. (2020). Optimal sizing of a Hybrid Renewable Energy System: Importance of data selection with highly variable renewable energy sources. *Energy Conversion and Management*, 223, 113303. <https://doi.org/10.1016/J.ENCONMAN.2020.113303>
- Amer, M., Namaane, A., & M'Sirdi, N. K. (2013). Optimization of hybrid renewable energy systems (HRES) using PSO for cost reduction. *Energy Procedia*, 42, 318–327. <https://doi.org/10.1016/J.EGYPRO.2013.11.032>
- Andy, T., Tameghe, T., & Wamkeue, R. (2015). Modelling and Simulation of a Flywheel Energy Storage System for Microgrids Power Plant Applications Active Disturbance rejection control and faults diagnosis of PV/Storage system (Experimentals and simulations tasks) View project NYPA-NYSERDA High-Performing Grid Grant View project.
- Bartolucci, L., Cordiner, S., Mulone, V., & Rossi, J. L. (2019). Hybrid renewable energy systems for household ancillary services. *International Journal of Electrical Power and Energy Systems*, 107, 282–297. <https://doi.org/10.1016/J.IJEPES.2018.11.021>
- Ben hmamou, D., Elyaqouti, M., Arjdal, E. hanafi, Saadaoui, D., Lidaighbi, S., Chaoufi, J., ... Obukhov, S. (2022). A novel hybrid numerical with analytical approach for parameter extraction of photovoltaic modules. *Energy Conversion and Management: X*, 14, 100219. <https://doi.org/10.1016/J.ECMX.2022.100219>
- Bérubé, J. F., Gendreau, M., & Potvin, J. Y. (2009). An exact ϵ -constraint method for bi-objective combinatorial optimization problems: Application to the Traveling Salesman Problem with Profits. *European Journal of Operational Research*, 194(1), 39–50. <https://doi.org/10.1016/J.EJOR.2007.12.014>
- Camargo, L. R., Nitsch, F., Gruber, K., Valdes, J., Wuth, J., & Dorner, W. (2019). Potential Analysis of Hybrid Renewable Energy Systems for Self-Sufficient Residential Use in Germany and the Czech Republic. *Energies 2019, Vol. 12, Page 4185*, 12(21), 4185. <https://doi.org/10.3390/EN12214185>
- Climate.OneBuilding.Org. (2022). Repository of free climate data for building performance simulation. Retrieved from https://climate.onebuilding.org/WMO_Region_1_Africa/KEN_Kenya/index.html
- Colmenar-Santos, A., Monteagudo-Mencucci, M., Rosales-Asensio, E., de Simón-Martín, M., & Pérez-Molina, C. (2019). Optimized design method for storage systems in photovoltaic plants with delivery limitation. *Solar Energy*, 180, 468–488. <https://doi.org/10.1016/J.SOLENER.2019.01.046>
- Come Zebra, E. I., van der Windt, H. J., Nhumaio, G., & Faaij, A. P. C. (2021). A review of hybrid renewable energy systems in mini-grids for off-grid electrification in developing countries. *Renewable and Sustainable Energy Reviews*, 144, 111036. <https://doi.org/10.1016/J.RSER.2021.111036>

- County, M. (2022). Theme for Increased household Income for Sustainable Livelihoods. Retrieved June 8, 2022, from <http://makueni.go.ke/planning/download/makueni-county-statistical-abstract-2021/>
- Dehghani, N. L., Zhang, C., & Shafieezadeh, A. (2021). Evolutionary optimization for resilience-based planning for power distribution networks. *Nature-Inspired Computing Paradigms in Systems*, 47–61. <https://doi.org/10.1016/B978-0-12-823749-6.00009-X>
- Duffie, J. A., Beckman, W. A., & McGowan, J. (1985). Solar Engineering of Thermal Processes. *American Journal of Physics*, 53(4), 382–382. <https://doi.org/10.1119/1.14178>
- Ellabban, O., Abu-Rub, H., & Blaabjerg, F. (2014). Renewable energy resources: Current status, future prospects and their enabling technology. *Renewable and Sustainable Energy Reviews*, 39, 748–764. <https://doi.org/10.1016/J.RSER.2014.07.113>
- EPRA. (2021). Energy-Petroleum-statistics-report-2021. Retrieved December 8, 2022, from <https://www.epra.go.ke/energy-petroleum-statistics-report-2021>
- Fadaee, M., & Radzi, M. A. M. (2012). Multi-objective optimization of a stand-alone hybrid renewable energy system by using evolutionary algorithms: A review. *Renewable and Sustainable Energy Reviews*, 16(5), 3364–3369. <https://doi.org/10.1016/J.RSER.2012.02.071>
- Fathima, A. H., & Palanisamy, K. (2015). Optimization in microgrids with hybrid energy systems – A review. *Renewable and Sustainable Energy Reviews*, 45, 431–446. <https://doi.org/10.1016/J.RSER.2015.01.059>
- Hasan, M. M., & Genç, G. (2022). Techno-economic analysis of solar/wind power based hydrogen production. *Fuel*, 324. <https://doi.org/10.1016/J.FUEL.2022.124564>
- Höök, M., & Tang, X. (2013). Depletion of fossil fuels and anthropogenic climate change—A review. *Energy Policy*, 52, 797–809. <https://doi.org/10.1016/J.ENPOL.2012.10.046>
- Huang, Q., Shi, Y., Wang, Y., Lu, L., & Cui, Y. (2015). Multi-turbine wind-solar hybrid system. *Renewable Energy*, 76, 401–407. <https://doi.org/10.1016/J.RENENE.2014.11.060>
- IEA, IRENA, UNSD, World Bank, W. (2022). Tracking SDG7: The Energy Progress Report - 2022. *Open Access*, 8(4), 2–263.
- Ishwarya, K., Yasoda, K., & Info, A. (2020). Maximum Power Point Tracking in Solar and Wind Hybrid Energy Conversion System. *International Journal for Modern Trends in Science and Technology*, 06, 159–164. <https://doi.org/10.46501/IJMTST060726>
- ITA. (2022). Kenya - Energy-Electrical Power Systems. Retrieved December 4, 2022, from <https://www.trade.gov/country-commercial-guides/kenya-energy-electrical-power-systems#>
- Jacob, E., & Farzaneh, H. (2022). Dynamic modeling and experimental validation of a standalone hybrid microgrid system in Fukuoka, Japan. *Energy Conversion and Management*, 274, 116462. <https://doi.org/10.1016/J.ENCONMAN.2022.116462>
- Kaabeche, A., & Ibtouen, R. (2014). Techno-economic optimization of hybrid photovoltaic/wind/diesel/battery generation in a stand-alone power system. *Solar Energy*, 103, 171–182. <https://doi.org/10.1016/J.SOLENER.2014.02.017>
- Kadri, T., Smaili, K., & Kadry, S. (2015). Markov Modeling for Reliability Analysis Using Hypoexponential Distribution. *Numerical Methods for Reliability and Safety Assessment*, 599–620. https://doi.org/10.1007/978-3-319-07167-1_23
- Kamjoo, A., Maheri, A., Dizqah, A. M., & Putrus, G. A. (2016). Multi-objective design under uncertainties of hybrid renewable energy system using NSGA-II and chance constrained programming. *International Journal of Electrical Power & Energy Systems*, 74, 187–194. <https://doi.org/10.1016/J.IJEPES.2015.07.007>
- Khan, M. F., Pervez, A., Modibbo, U. M., Chauhan, J., & Ali, I. (2021). Flexible Fuzzy Goal Programming Approach in Optimal Mix of Power Generation for Socio-Economic

- Sustainability: A Case Study. *Sustainability* 2021, Vol. 13, Page 8256, 13(15), 8256. <https://doi.org/10.3390/SU13158256>
- Kovalev, K., Poltavets, V., & Kolchanova, I. (2019). Flywheel energy storage systems for autonomous energy systems with renewable energy sources. *IOP Conference Series: Materials Science and Engineering*, 643(1). <https://doi.org/10.1088/1757-899X/643/1/012106>
- Mahmoud, F. S., Diab, A. A. Z., Ali, Z. M., El-Sayed, A. H. M., Alquthami, T., Ahmed, M., & Ramadan, H. A. (2022). Optimal sizing of smart hybrid renewable energy system using different optimization algorithms. *Energy Reports*, 8, 4935–4956. <https://doi.org/10.1016/J.EGYR.2022.03.197>
- Mavrotas, G. (2009). Effective implementation of the ϵ -constraint method in Multi-Objective Mathematical Programming problems. *Applied Mathematics and Computation*, 213(2), 455–465. <https://doi.org/10.1016/J.AMC.2009.03.037>
- Michanan, J., Dewri, R., & Rutherford, M. J. (2015). Understanding the power-performance tradeoff through Pareto analysis of live performance data. *2014 International Green Computing Conference, IGCC 2014*. <https://doi.org/10.1109/IGCC.2014.7039164>
- Olabi, A. G., Wilberforce, T., Abdelkareem, M. A., & Ramadan, M. (2021). Critical Review of Flywheel Energy Storage System. *Energies* 2021, Vol. 14, Page 2159, 14(8), 2159. <https://doi.org/10.3390/EN14082159>
- Pang, M., Shi, Y., Wang, W., & Pang, S. (2019). Optimal sizing and control of hybrid energy storage system for wind power using hybrid Parallel PSO-GA algorithm. *Energy Exploration & Exploitation*, 37(1), 558–578. <https://doi.org/10.1177/0144598718784036>
- Projects, M. (2022). Case study: How a DC microgrid helps over 10,000 Kenyan tea growers bring their product to market. Retrieved December 4, 2022, from <https://www.microgridknowledge.com/resources/microgrid-case-studies/article/11437319/alcon-systems-case-study-how-a-dc-microgrid-helps-over-10000-kenyan-tea-growers-bring-their-product-to-market>
- Ramli, M. A. M., Boucekara, H. R. E. H., & Alghamdi, A. S. (2018). Optimal sizing of PV/wind/diesel hybrid microgrid system using multi-objective self-adaptive differential evolution algorithm. *Renewable Energy*, 121, 400–411. <https://doi.org/10.1016/J.RENENE.2018.01.058>
- Ramos, M. A., Boix, M., Montastruc, L., & Domenech, S. (2014). Multiobjective Optimization Using Goal Programming for Industrial Water Network Design. <https://doi.org/10.1021/ie5025408>
- Reinders, A., Moser, D., Sark, W. Van, Oreski, G., Pearsall, N., Scognamiglio, A., & Leloux, J. (2018). Introducing “PEARL-PV”: Performance and Reliability of Photovoltaic Systems: Evaluations of Large-Scale Monitoring Data. In *2018 IEEE 7th World Conference on Photovoltaic Energy Conversion, WCPEC 2018 - A Joint Conference of 45th IEEE PVSC, 28th PVSEC and 34th EU PVSEC* (pp. 762–766). <https://doi.org/10.1109/PVSC.2018.8547966>
- Saleh, A., Awad, A., & Ghanem, W. (2019). Modeling, Control, and Simulation of a New Topology of Flywheel Energy Storage Systems in Microgrids. *IEEE Access*, 7, 160363–160376. <https://doi.org/10.1109/ACCESS.2019.2951029>
- Shaqour, A., Farzaneh, H., Yoshida, Y., & Hinokuma, T. (2020). Power control and simulation of a building integrated stand-alone hybrid PV-wind-battery system in Kasuga City, Japan. *Energy Reports*, 6, 1528–1544. <https://doi.org/10.1016/J.EGYR.2020.06.003>
- Sharma, R., Kodamana, H., & Ramteke, M. (2022). Multi-objective dynamic optimization of hybrid renewable energy systems. *Chemical Engineering and Processing - Process Intensification*, 170, 108663. <https://doi.org/10.1016/J.CEP.2021.108663>
- Singh, R., Bansal, R. C., Singh, A. R., & Naidoo, R. (2018). Multi-Objective Optimization of

- Hybrid Renewable Energy System Using Reformed Electric System Cascade Analysis for Islanding and Grid Connected Modes of Operation. *IEEE Access*, 6, 47332–47354. <https://doi.org/10.1109/ACCESS.2018.2867276>
- Su, W., Jin, T., & Wang, S. (2010). Modeling and simulation of short-term energy storage: Flywheel. *2010 International Conference on Advances in Energy Engineering, ICAEE 2010*, 9–12. <https://doi.org/10.1109/ICAEE.2010.5557629>
- Yang, H., Zhou, W., Lu, L., & Fang, Z. (2008). Optimal sizing method for stand-alone hybrid solar–wind system with LPSP technology by using genetic algorithm. *Solar Energy*, 82(4), 354–367. <https://doi.org/10.1016/J.SOLENER.2007.08.005>
- Yazdanpanah, M. A. (2014). Modeling and sizing optimization of hybrid photovoltaic/wind power generation system. *Journal of Industrial Engineering International*, 10(1). <https://doi.org/10.1007/s40092-014-0049-7>
- Zhang, N., Yang, N. C., & Liu, J. H. (2021). Optimal Sizing of PV/Wind/Battery Hybrid Microgrids Considering Lifetime of Battery Banks. *Energies 2021, Vol. 14, Page 6655*, 14(20), 6655. <https://doi.org/10.3390/EN14206655>
- Zhang, W., Maleki, A., Rosen, M. A., & Liu, J. (2018). Optimization with a simulated annealing algorithm of a hybrid system for renewable energy including battery and hydrogen storage. *Energy*, 163, 191–207. <https://doi.org/10.1016/J.ENERGY.2018.08.112>